

2014

Exclusive $\pi(0)$ electroproduction at $W > 2$ GeV with CLAS

N. A. Baltzell

A. El Alaoui

K. Hafidi

K. A. Griffioen

College of William and Mary

Follow this and additional works at: <https://scholarworks.wm.edu/aspubs>

Recommended Citation

Bedlinskiy, I., Kubarovsky, V., Niccolai, S., Stoler, P., Adhikari, K. P., Anderson, M. D., ... & Battaglieri, M. (2014). Exclusive π^0 electroproduction at $W > 2$ GeV with CLAS. *Physical Review C*, 90(2), 025205.

This Article is brought to you for free and open access by the Arts and Sciences at W&M ScholarWorks. It has been accepted for inclusion in Arts & Sciences Articles by an authorized administrator of W&M ScholarWorks. For more information, please contact scholarworks@wm.edu.

1
 2 I. Bedlinskiy,¹⁹ V. Kubarovsky,^{32,27} S. Niccolai,^{18,12} P. Stoler,²⁷ K.P. Adhikari,²⁶ M.D. Anderson,³⁵
 3 S. Anefalos Pereira,¹⁵ H. Avakian,³² J. Ball,⁶ N.A. Baltzell,^{1,31} M. Battaglieri,¹⁶ V. Batourine,^{32,21}
 4 A.S. Biselli,⁹ S. Boiarinov,³² J. Bono,¹⁰ W.J. Briscoe,¹² W.K. Brooks,^{33,32} V.D. Burkert,³² D.S. Carman,³²
 5 A. Celentano,¹⁶ S. Chandavar,²⁵ L. Colaneri,¹⁷ P.L. Cole,¹³ M. Contalbrigo,¹⁴ O. Cortes,¹³ V. Crede,¹¹
 6 A. D'Angelo,^{17,29} N. Dashyan,³⁹ R. De Vita,¹⁶ E. De Sanctis,¹⁵ A. Deur,³² C. Djalali,³¹ D. Doughty,^{7,32}
 7 R. Dupre,¹⁸ H. Egiyan,^{32,23} A. El Alaoui,^{1,*} L. El Fassi,²⁶ L. Elouadrhiri,³² P. Eugenio,¹¹ G. Fedotov,^{31,30}
 8 S. Fegan,¹⁶ J.A. Fleming,³⁴ T.A. Forest,¹³ B. Garillon,¹⁸ M. Garçon,⁶ G. Gavalian,²⁶ N. Gevorgyan,³⁹
 9 Y. Ghandilyan,³⁹ G.P. Gilfoyle,²⁸ K.L. Giovanetti,²⁰ F.X. Girod,^{32,6} E. Golovatch,³⁰ R.W. Gothe,³¹
 10 K.A. Griffioen,³⁸ B. Guegan,¹⁸ L. Guo,^{10,32} K. Hafidi,¹ H. Hakobyan,^{33,39} N. Harrison,⁸ M. Hattawy,¹⁸
 11 K. Hicks,²⁵ M. Holtrop,²³ D.G. Ireland,³⁵ B.S. Ishkhanov,³⁰ E.L. Isupov,³⁰ D. Jenkins,³⁶ H.S. Jo,¹⁸ K. Joo,⁸
 12 D. Keller,³⁷ M. Khandaker,^{13,24} A. Kim,⁸ W. Kim,²¹ A. Klein,²⁶ F.J. Klein,⁵ S. Koirala,²⁶ S.E. Kuhn,²⁶
 13 S.V. Kuleshov,^{33,19} P. Lenisa,¹⁴ W.I. Levine,⁴ K. Livingston,³⁵ H.Y. Lu,³¹ I. J. D. MacGregor,³⁵
 14 N. Markov,⁸ M. Mayer,²⁶ B. McKinnon,³⁵ M. Mirazita,¹⁵ V. Mokeev,^{32,30} R.A. Montgomery,^{15,†}
 15 C.I. Moody,¹ H. Moutarde,⁶ A. Movsisyan,¹⁴ C. Munoz Camacho,¹⁸ P. Nadel-Turonski,^{32,12} I. Niculescu,²⁰
 16 M. Osipenko,¹⁶ A.I. Ostrovidov,¹¹ L.L. Pappalardo,¹⁴ K. Park,^{32,21} S. Park,¹¹ E. Pasyuk,³²
 17 E. Phelps,³¹ W. Phelps,¹⁰ J.J. Phillips,³⁵ S. Pisano,¹⁵ O. Pogorelko,¹⁹ J.W. Price,³ Y. Prok,^{26,32,37}
 18 D. Protopopescu,³⁵ S. Procureur,⁶ A.J.R. Puckett,⁸ B.A. Raue,^{10,32} M. Ripani,¹⁶ B.G. Ritchie,²
 19 A. Rizzo,^{17,‡} P. Rossi,^{15,32} P. Roy,¹¹ F. Sabatié,⁶ C. Salgado,²⁴ D. Schott,¹² R.A. Schumacher,⁴
 20 E. Seder,⁸ I. Senderovich,² Y.G. Sharabian,³² A. Simonyan,³⁹ G.D. Smith,^{34,†} D.I. Sober,⁵
 21 D. Sokhan,^{35,18} S.S. Stepanyan,²¹ S. Strauch,^{31,12} V. Sytnik,³³ W. Tang,²⁵ Ye Tian,³¹ M. Ungaro,^{32,8}
 22 A.V. Vlassov,¹⁹ H. Voskanyan,³⁹ E. Voutier,²² N.K. Walford,⁵ D. Watts,³⁵ X. Wei,³² L.B. Weinstein,²⁶
 23 M. Yurov,³⁷ N. Zachariou,³¹ L. Zana,^{34,23} J. Zhang,^{32,26} Z.W. Zhao,^{37,31} and I. Zonta^{17,‡}

(The CLAS Collaboration)

¹Argonne National Laboratory, Argonne, Illinois 60439

²Arizona State University, Tempe, Arizona 85287-1504

³California State University, Dominguez Hills, Carson, CA 90747

⁴Carnegie Mellon University, Pittsburgh, Pennsylvania 15213

⁵Catholic University of America, Washington, D.C. 20064

⁶CEA, Centre de Saclay, Irfu/Service de Physique Nucléaire, 91191 Gif-sur-Yvette, France

⁷Christopher Newport University, Newport News, Virginia 23606

⁸University of Connecticut, Storrs, Connecticut 06269

⁹Fairfield University, Fairfield CT 06824

¹⁰Florida International University, Miami, Florida 33199

¹¹Florida State University, Tallahassee, Florida 32306

¹²The George Washington University, Washington, DC 20052

¹³Idaho State University, Pocatello, Idaho 83209

¹⁴INFN, Sezione di Ferrara, 44100 Ferrara, Italy

¹⁵INFN, Laboratori Nazionali di Frascati, 00044 Frascati, Italy

¹⁶INFN, Sezione di Genova, 16146 Genova, Italy

¹⁷INFN, Sezione di Roma Tor Vergata, 00133 Rome, Italy

¹⁸Institut de Physique Nucléaire ORSAY, Orsay, France

¹⁹Institute of Theoretical and Experimental Physics, Moscow, 117218, Russia

²⁰James Madison University, Harrisonburg, Virginia 22807

²¹Kyungpook National University, Daegu 702-701, Republic of Korea

²²LPSC, Université Joseph Fourier, CNRS/IN2P3, INPG, Grenoble, France

²³University of New Hampshire, Durham, New Hampshire 03824-3568

²⁴Norfolk State University, Norfolk, Virginia 23504

²⁵Ohio University, Athens, Ohio 45701

²⁶Old Dominion University, Norfolk, Virginia 23529

²⁷Rensselaer Polytechnic Institute, Troy, New York 12180-3590

²⁸University of Richmond, Richmond, Virginia 23173

²⁹Università di Roma Tor Vergata, 00133 Rome Italy

³⁰Skobeltsyn Institute of Nuclear Physics, Lomonosov Moscow State University, 119234 Moscow, Russia

³¹University of South Carolina, Columbia, South Carolina 29208

³²Thomas Jefferson National Accelerator Facility, Newport News, Virginia 23606

³³Universidad Técnica Federico Santa María, Casilla 110-V Valparaíso, Chile

³⁴Edinburgh University, Edinburgh EH9 3JZ, United Kingdom

³⁵University of Glasgow, Glasgow G12 8QQ, United Kingdom

³⁶Virginia Polytechnic Institute and State University, Blacksburg, Virginia 24061-0435

Exclusive neutral-pion electroproduction ($ep \rightarrow e'p'\pi^0$) was measured at Jefferson Lab with a 5.75-GeV electron beam and the CLAS detector. Differential cross sections $d^4\sigma/dtdQ^2dx_Bd\phi_\pi$ and structure functions $\sigma_T + \epsilon\sigma_L, \sigma_{TT}$ and σ_{LT} as functions of t were obtained over a wide range of Q^2 and x_B . The data are compared with Regge and handbag theoretical calculations. Analyses in both frameworks find that a large dominance of transverse processes is necessary to explain the experimental results. For the Regge analysis it is found that the inclusion of vector meson rescattering processes is necessary to bring the magnitude of the calculated and measured structure functions into rough agreement. In the handbag framework, there are two independent calculations, both of which appear to roughly explain the magnitude of the structure functions in terms of transversity generalized parton distributions.

I. INTRODUCTION

Understanding nucleon structure in terms of the fundamental degrees of freedom of Quantum Chromodynamics (QCD) is one of the main goals in the theory of strong interactions. The nucleon is a many-body system of quarks and gluons. How partons move and how they are distributed in space is still an open question on which new theoretical and experimental developments are starting to shed a new light. The study of deep inelastic scattering provides the distribution of longitudinal momentum and polarization carried by quarks and antiquarks within the fast moving hadron. However, the spatial distribution of the partons in the plane perpendicular to the hadron motion is not accessible in these experiments. The role of the partons' orbital angular momenta in making up the total spin of the nucleon is one more unresolved question. In recent years it became clear that exclusive reactions may provide such information encoded in so-called Generalized Parton Distributions (GPDs) [1, 2]. The GPDs describe the simultaneous distribution of partons with respect to both the partons' transverse positions and longitudinal momenta. In addition to the information about transverse spatial density (form factors) and momentum density, these functions reveal the correlation of the spatial and momentum distributions, i.e. how the spatial shape of the nucleon changes when probing quarks of different longitudinal momenta. GPDs give access as well to the total angular momentum carried by partons, comprising the spin and orbital parts [1].

The possibility to study GPDs in exclusive scattering processes rests on factorization theorems, which are proven for virtual Compton scattering [3] and light meson electroproduction [4] in the limit of $Q^2 \rightarrow \infty$, at fixed x_B and t . Here, $q^2 \equiv -Q^2$ is the square of the 4-momentum transferred to the hadronic system by the scattered electron, $-t$ is the 4-momentum transferred to the recoiling proton and x_B is the Bjorken variable. These proofs are based on the properties of matrix elements represented by Feynman diagrams colloquially referred to as handbags [1, 2, 5]. The reaction is factorized into two parts. One part treats the elementary interaction

with one of the partons in the nucleon perturbatively, while the non-perturbative remainder is embodied in GPDs. While the perturbative process between the virtual photon and the quark is reaction dependent, the information contained within the GPDs is universal. Figure 1 indicates the lowest order handbag mechanism applied to three reactions: elastic scattering, deeply virtual Compton scattering (DVCS) and deeply virtual meson electroproduction (DVMP), which is the subject of this article.

While the handbag mechanism should be mostly applicable at asymptotically large photon virtuality Q^2 , there is some experimental evidence [6] that the DVCS reaction at Q^2 as low as 1.5 GeV² appears to be applicable by the handbag mechanism. This is not unexpected since both vertices of the Compton scattering reaction from a single quark involve perturbative electromagnetic processes. On the other hand, for DVMP, the second vertex (πqq in the right plot of Fig. 1) involves the exchange of at least one gluon, and the kinematic range of leading-order applicability of the handbag formalism is not as clearly determined.

There are eight GPDs. Four correspond to parton helicity-conserving (chiral-even) processes, denoted by H^q, \tilde{H}^q, E^q and \tilde{E}^q , and four correspond to parton helicity-flip (chiral-odd) processes [7, 8], $H_T^q, \tilde{H}_T^q, E_T^q$ and \tilde{E}_T^q . At a given Q^2 the GPDs depend on three kinematic variables: x, ξ and t . In a symmetric frame, x is the average longitudinal momentum fraction of the struck parton before and after the hard interaction and ξ (skewness) is half of the longitudinal momentum fraction transferred to the struck parton. The skewness can be expressed in terms of the Bjorken variable x_B as $\xi \simeq x_B/(2-x_B)$. Here $x_B = Q^2/(2p \cdot q)$ and $t = (p-p')^2$, where p and p' are the initial and final four-momenta of the nucleon. The GPDs encode both the longitudinal momentum distributions through their dependence on x and the transverse position distributions through their dependence on t .

In the forward limit where $t \rightarrow 0$, H^q and \tilde{H}^q reduce to the parton density distributions $q(x)$ and parton helicity distributions $\Delta q(x)$, respectively. The first moments in x of the chiral-even GPDs are

*Current address:Universidad Técnica Federico Santa María, Casilla 110-V Valparaíso, Chile

†Current address:University of Glasgow, Glasgow G12 8QQ, United Kingdom

‡Current address:Universita' di Roma Tor Vergata, 00133 Rome Italy

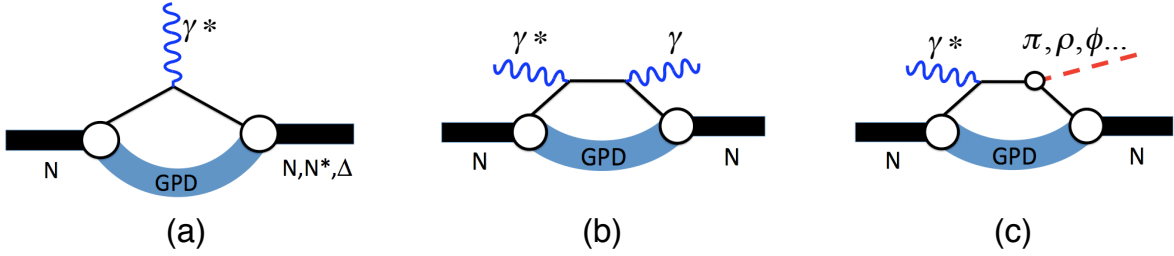


FIG. 1: (Color online) Schematic diagram of the lowest order handbag mechanism applied to: (left) elastic scattering, (middle) DVCS and (right) meson production.

1 related to the elastic form factors of the nucleon: 25
 2 the Dirac form factor $F_1^q(t)$, the Pauli form factor 26
 3 $F_2^q(t)$, the axial-vector form factor $g_A^q(t)$ and the 27
 4 pseudoscalar form factor $h_A^q(t)$ [9]. 28

5 The DVMP process specifically for π^0 production 29
 is shown in more detail in Fig. 2. 30

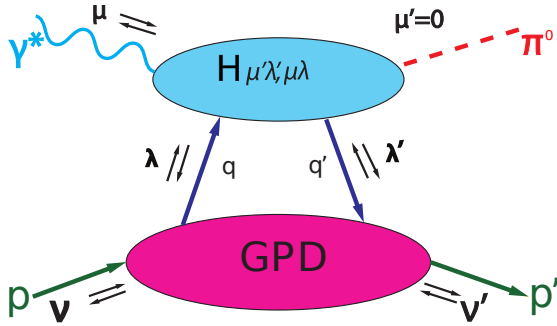


FIG. 2: (Color online) Schematic diagram of the π^0 electroproduction amplitude in the framework of the handbag mechanism. The helicities of the initial and final nucleons are denoted by ν and ν' , of the incident photon and produced meson by μ and μ' and of the active initial and final quark by λ and λ' . The arrows in the figure schematically represent the corresponding positive and negative helicities, respectively. For final-state photons or vector mesons $\mu' = \pm 1$, while for pseudoscalar mesons $\mu' = 0$.

6
 7 It was shown early-on [10] that for pion electro-
 8 production the leading handbag approach is valid
 9 at large Q^2 for longitudinal helicity-conserving
 10 virtual photons. Using Regge phenomenology as a
 11 guide for parametrization of the four longitudinal
 12 GPDs, Refs. [11, 12] calculated cross-section structure
 13 functions for longitudinal helicity-conserving
 14 virtual photons. Simultaneously, the CLAS Collab-
 15 oration as well as other groups [13–15], measured
 16 the differential cross sections for pion electroproduc-
 17 tion and extracted structure functions, which are
 18 the subject of the present paper. When the theo-
 19 retical calculations for longitudinal virtual photons
 20 were compared with the JLab data, as well as with
 21 HERMES data, they were found to underestimate
 22 the measured cross sections by more than an order
 23 of magnitude in their accessible kinematic regions,
 24 even after including finite-size corrections through

Sudakov form factors [12]. At JLab, sizeable beam-
 spin asymmetries for exclusive neutral pion electro-
 production off the proton were measured [16] above
 the resonance region. These non-zero asymmetries
 imply that both transverse and longitudinal ampli-
 tudes participate in the process.

31 The failure to describe the experimental results
 32 with quark helicity-conserving operators [9, 11]
 33 stimulated a consideration of the role of the chiral-
 34 odd quark helicity-flip processes. Pseudoscalar meson
 35 electroproduction, and in particular π^0 produc-
 36 tion in the reaction $ep \rightarrow e'p'\pi^0$, was identi-
 37 fied [12, 17, 18] as especially sensitive to the quark
 38 helicity-flip subprocesses. The produced meson has
 39 no intrinsic helicity so that the angular momentum
 40 of the incident photon is either transferred to the
 41 nucleon via a quark helicity-flip or involves orbital
 42 angular momentum processes. Evidence of the con-
 43 tribution of helicity-flip subprocesses, especially H_T ,
 44 to π^+ electroproduction in transverse target spin
 45 asymmetry data [15] was noted in Ref. [12]. A dis-
 46 advantage of π^+ production is that the interpreta-
 47 tion is complicated by the dominance of the longi-
 48 tudinal π^+ -pole term, which is absent in π^0 produc-
 49 tion. In addition, for π^0 production the structure of
 50 the amplitudes further suppresses the quark helicity-
 51 conserving amplitudes relative to the helicity-flip
 52 amplitudes [12]. On the other hand, π^0 cross sec-
 53 tions over a large kinematic range are much more
 54 difficult to obtain than for π^+ since the clean detec-
 55 tion of π^0 s requires the measurement of their two
 56 decay photons.

57 During the past few years, two parallel theoretical
 58 approaches - [17, 19] (GL) and [12, 18] (GK) have
 59 been developed utilizing the chiral-odd GPDs in the
 60 calculation of pseudoscalar meson electroproduction.
 61 The GL and GK approaches, though employing dif-
 62 ferent models of GPDs, lead to *transverse* photon
 63 amplitudes that are much larger than the longitudi-
 64 nal amplitudes.

65 At the same time the most successful theoretical
 66 approaches for describing exclusive reactions in the
 67 past have been those based upon the Regge model,
 68 which was introduced in the 1960's. The Regge
 69 model [20] has continued to provide insights into the
 70 nature of hadrons and their interactions.

1 The comparison of the results of GL and GK with
 2 each other and with the results obtained by the anal-
 3 ysis of some of the CLAS data was discussed in
 4 Ref. [13].

5 This paper presents the complete results of that
 6 experiment and a comprehensive description of the
 7 data analysis, following the description of the exper-
 8 iment. The experimental results will be compared
 9 with those of G-L and G-K as well as with the most
 10 advanced Regge model predictions [20] for the π^0 ex-
 11 clusive production over a wider range of kinematic
 12 intervals than previously available.

13 The main goal of the experiment was to measure
 14 the differential cross section $\frac{d^4\sigma}{dQ^2 dx_B dt d\phi_\pi}$ of the reac-
 15 tion $ep \rightarrow e'p'\pi^0$ in bins of Q^2 , x_B , t and ϕ_π , where
 16 ϕ_π is the angle of the final-state hadronic plane re-
 17 lative to the electron scattering plane. Fits to the ϕ_π
 18 dependence (see Appendix B Eq. B1), in each bin of
 19 Q^2 , x_B and t , give access to the structure functions
 20 ($\sigma_T + \epsilon\sigma_L$), σ_{TT} and σ_{LT} .

21 II. EXPERIMENTAL SETUP

22 The measurements reported here were carried out
 23 with the CEBAF Large Acceptance Spectrometer
 24 (CLAS) [21] located in Hall B at Jefferson Lab. A
 25 three-dimensional view of CLAS with the different
 26 subsystems labeled is shown in Fig. 3. The data were
 27 taken with a 5.75-GeV electron beam and a 2.5-cm-
 28 long liquid-hydrogen target. The target was placed
 29 66 cm upstream of the nominal center of CLAS in-
 30 side a solenoid magnet to shield the detectors from
 31 Møller electrons. The spectrometer was operated
 32 at an instantaneous luminosity of $2 \times 10^{34} \text{ cm}^{-2}\text{s}^{-1}$.
 33 The scheme of the CLAS geometry, as coded in
 34 the GEANT3-based CLAS simulation code GSIM,
 35 is shown in Fig. 4. CLAS consisted of six identi-
 36 cal sectors with an approximately toroidal magnetic
 37 field. Each sector was equipped with three regions of
 38 drift chambers (DC) [22] to determine the trajectory
 39 of charged particles, gas threshold Cherenkov coun-
 40 ters (CC) [23] for electron identification, a scintilla-
 41 tion hodoscope [24] for time-of-flight (TOF) mea-
 42 surement of charged particles and an electromag-
 43 netic calorimeter (EC) [25] which was used for elec-
 44 tron identification as well as detection of neutral par-
 45 ticles. To detect photons at small polar angles (from
 46 4.5° up to 17°) an inner calorimeter (IC) was added
 47 to the standard CLAS configuration, 55 cm down-
 48 stream from the target. Figure 5 zooms in on the tar-
 49 get area of Fig. 4 to better illustrate the deployment
 50 of the IC and solenoid relative to the target. The IC
 51 consisted of 424 PbWO_4 tapered crystals whose ori-
 52 entations were projected somewhat upstream of the
 53 target. Each crystal had a $13.3 \times 13.3 \text{ mm}^2$ square
 54 front face, a $16 \times 16 \text{ mm}^2$ rear face and 160 mm of
 55 length. The light from each crystal was collected
 56 with an avalanche photo-diode followed by a low-
 57 noise preamplifier. The temperature of the IC was

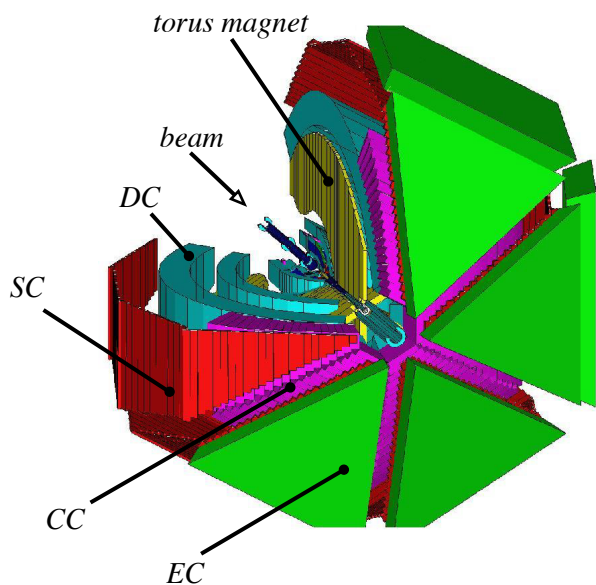


FIG. 3: (Color online) Three-dimensional schematic view of the elements of the CLAS detector with the different subsystems labeled. A single sector of the detector has been cut away to enable a view of the inner subsystems. The diameter of the CLAS detector is ~ 10 m. The notation is as follows: EC—Electromagnetic Calorimeter, CC—Cherenkov Counter, SC—Scintillation hodoscope, DC—Drift Chambers.

stabilized with $< 0.1^\circ\text{C}$ precision. The toroidal magnet was operated at a current corresponding to an integral magnetic field of about 1.36 T-m in the forward direction. The magnet polarity was set such that negatively charged particles were bent inward towards the electron beam line. The scattered electrons were detected in the CC and EC, which extended from 21° to 45° . The lower limit was defined by the IC calorimeter located just after the target. A totally-absorbing Faraday cup was used to determine the integrated beam charge passing through the target.

In the experiment, all four final state particles of the reaction $ep \rightarrow e'p'\pi^0$, $\pi^0 \rightarrow \gamma\gamma$ were detected. The kinematic coverage for this reaction is shown in Fig. 6, and for the individual kinematic variables in Fig. 7. For the purpose of physics analysis an additional cut on $W > 2 \text{ GeV}$ was applied as well, where W is the γ^*p center-of-mass energy.

The basic configuration of the trigger included the coincidence between signals from two detectors in the same sector: the CC and the EC with a threshold $\sim 500 \text{ MeV}$. Out of a total of about 7×10^9 recorded events, about 1×10^5 events for the reaction of interest were finally retained. The specific experimental data set (“e1-dvcs”) used for this analysis was collected in 2005. The integrated luminosity collected was 31.4 fb^{-1} . However, not all data were used for the measurement of the cross section. After applying strict run-to-run stability criteria, the integrated luminosity corresponding to the data presented here

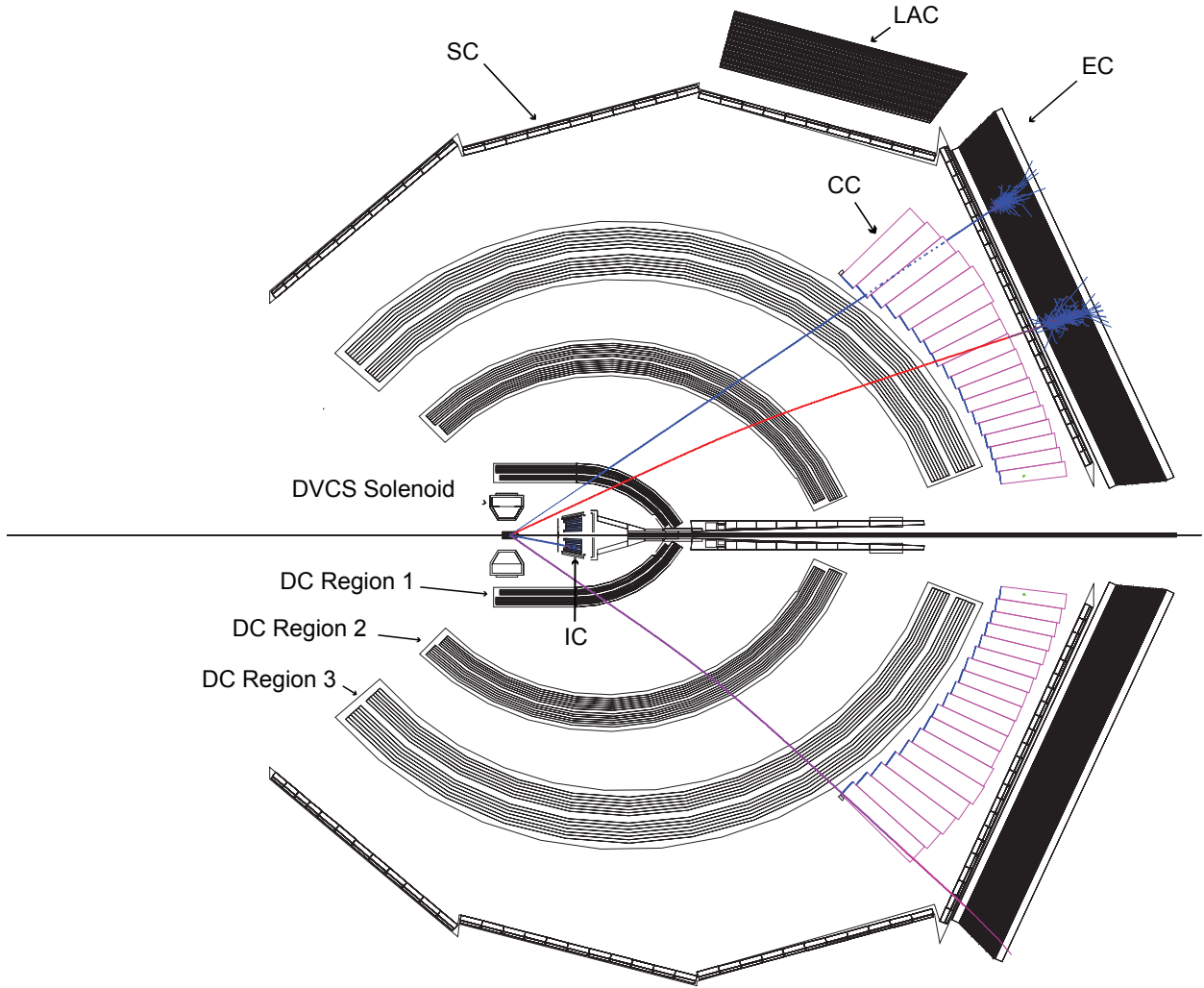


FIG. 4: (Color online) Schematic view of the CLAS detector constructed by the Monte-Carlo simulation program GSIM. Note, IC–inner calorimeter, EC–electromagnetic calorimeter, LAC–large angle electromagnetic calorimeter, CC–Cherenkov counter, SC–scintillation hodoscope, DC–Drift Chambers. The LAC was not used in this analysis. The tracks correspond, from top to bottom, to a photon (blue online), an electron (red online) curving toward the beam line, and a proton (purple online) curving away from the beam line.

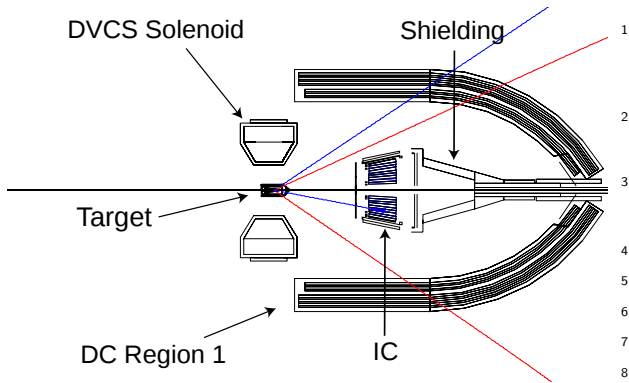


FIG. 5: (Color online) A blowup of Fig. 4 showing the CLAS target region in detail. IC is the inner calorimeter and DC-region 1 represents the drift chambers closest to the target.

1 was was 19.9 fb^{-1} .

III. PARTICLE IDENTIFICATION

A. Electron Identification

2
3
4 An electron was identified by requiring the track
5 of a negatively charged particle in the DCs to be
6 matched in time and space with hits in the CC, the
7 EC and the SC in the same sector of CLAS. This
8 electron selection effectively suppresses π^- contam-
9 ination up to momenta $\sim 2.5 \text{ GeV}$. Additional re-
10 quirements were used in the offline analysis to refine
11 electron identification and to suppress the remain-
12 ing pions. Geometric “fiducial” cuts were applied in
13 such a way that only regions in the CC and EC that
14 had high electron efficiency were used.

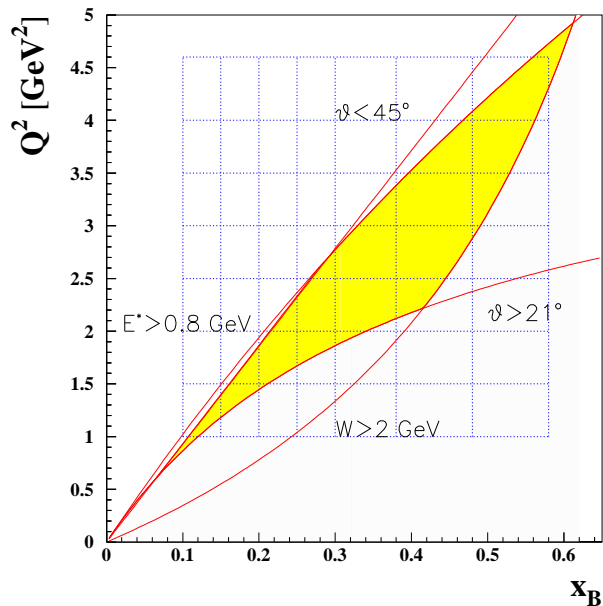


FIG. 6: (Color online) The kinematic coverage and binning as a function of Q^2 and x_B . The accepted region (yellow online) is determined by the following cuts: $W > 2$ GeV, $E' > 0.8$ GeV, $21^\circ < \theta < 45^\circ$. W is the γ^*p center-of-mass energy, E' is the scattered electron energy and θ is the electron's polar angle in the lab frame. The dotted grid represents the kinematic regions for which the cross sections are calculated and presented.

Energy deposition cuts on the electron signal in the EC also play an important role in suppressing background. An electron propagating through the calorimeter produces an electromagnetic shower and deposits a large fraction of its energy in the calorimeter proportional to its momentum, while pions typically lose a smaller fraction of their energy primarily by ionization. For an electron, the observed energy to momentum ratio E_{cal}/p is known as the sampling fraction. The observed sampling fraction vs. momentum is shown in Fig. 8. The electron events are broadly clustered near $E_{cal}/p \sim 0.25$. A cut was then applied to select events within the cluster area. As shown in Fig. 8, a $\pm 3.5\sigma$ sampling fraction cut was used in this analysis.

The distribution of the number of the photoelectrons in the CC is shown in Fig. 9. The upper panel shows the distribution before the various cuts such as EC sampling fraction, and angle and geometry matching between the electron track and the hits in the CC. The peak around $N_{phe} = 1$ represents the pion contamination. The lower panel shows the same distribution after these cuts and the selection of the exclusive reaction (see Section IV B). The single photoelectron peak becomes negligibly small.

The charged particle tracks were reconstructed by the drift chambers. The vertex location was calculated by the intersection of the track with the beamline. A cut was applied on the z -component of the

electron vertex position to eliminate events originating outside the target. The vertex distribution and cuts for one of the sectors is shown in Fig. 10. The left plot shows the z -coordinate distribution before the exclusivity cuts, which are described below in Section IV B, and the right plot is the distribution after the exclusivity cuts. The peak at $z = -62.5$ cm exhibits the interaction of the beam with an insulating foil. It is completely removed after the exclusivity cuts, demonstrating that these cuts very effectively exclude the interactions involving nuclei of the surrounding non-target material.

B. Proton identification

The proton was identified as a positively charged particle with the correct time-of-flight. The quantity of interest ($\delta t = t_{SC} - t_{exp}$) is the difference in the time between the measured flight time from the event vertex to the SC system (t_{SC}) and that expected for the proton (t_{exp}). The quantity t_{exp} was computed from the velocity of the particle and the track length. The velocity was determined from the momentum assuming the mass of the particle equals that of a proton. A cut at the level of $\pm 5\sigma_t$ was applied around $\delta t = 0$, where σ_t is the time-of-flight resolution. Such a wide cut is possible because the exclusivity cuts very effectively suppressed the remaining pion contamination.

C. Photon identification

Photons were detected in both calorimeters, the EC and IC. In the EC, photons were identified as *neutral* particles with $\beta > 0.8$ and $E > 0.35$ GeV. Fiducial cuts were applied to avoid the EC edges. When a photon hits the boundary of the calorimeter, the energy cannot be fully reconstructed due to the leakage of the shower out of the detector. Additional fiducial cuts on the EC were applied to account for the shadow of the IC (see Fig. 4). The calibration of the EC was done using cosmic muons and the photons from neutral pion decay ($\pi^0 \rightarrow \gamma\gamma$).

In the IC each detected cluster was considered a photon. The assumption was made that this photon originated from the electron vertex. Additional geometric cuts were applied to remove low-energy clusters around the beam axis and photons near the edges of the IC, where the energies of the photons were incorrectly reconstructed due to the electromagnetic shower leakage. The photons from $\pi^0 \rightarrow \gamma\gamma$ decays were detected in the IC in an angular range between 5° and 17° and in the EC for angles greater than 21° . The reconstructed invariant mass of two-photon events was then subjected to various cuts to isolate exclusive π^0 events, with a small residual background, as discussed in the section on exclusivity cuts in Sec. IV B below.

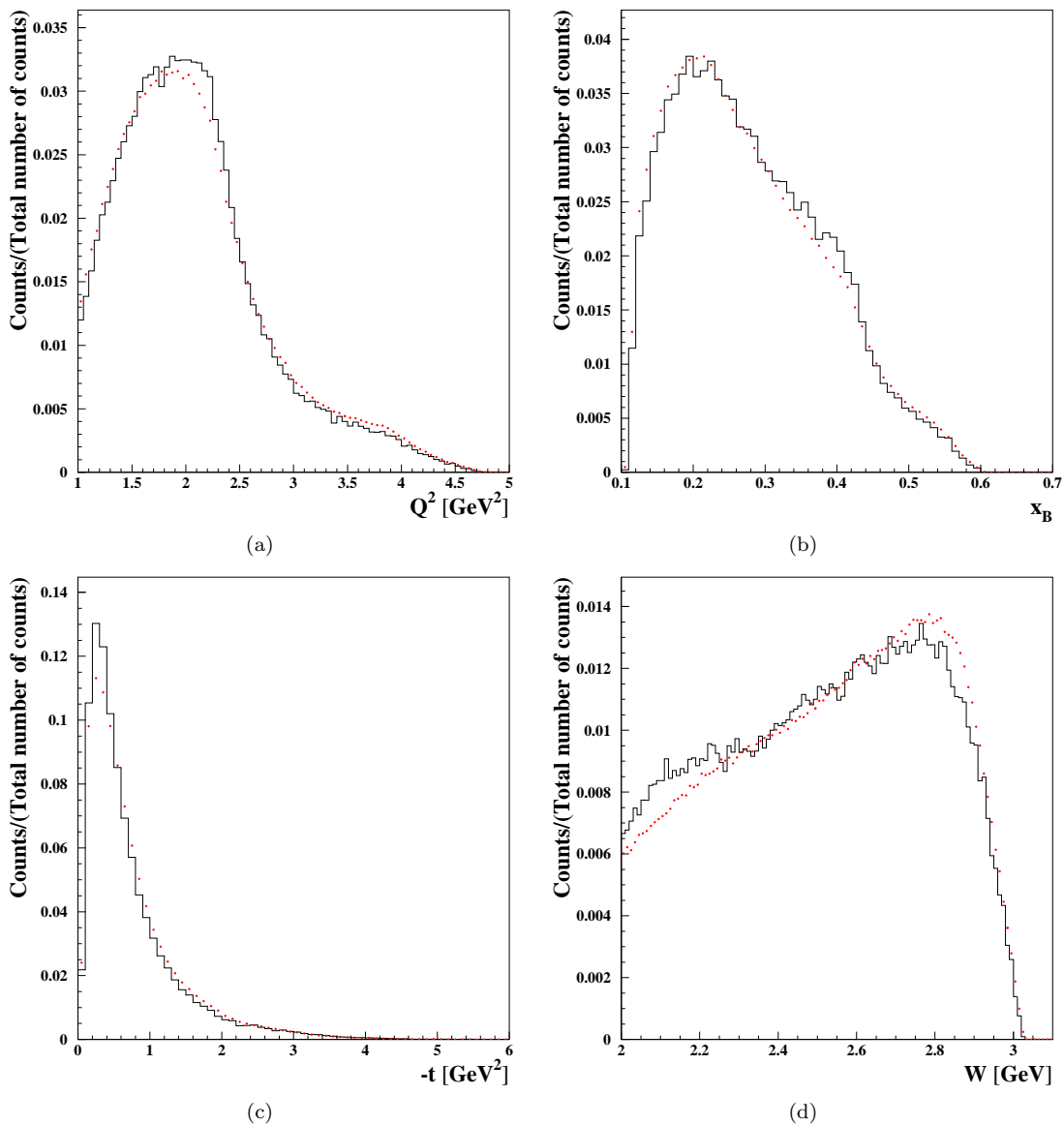


FIG. 7: (Color online) Distributions for kinematic variables Q^2 (a), x_B (b), $-t$ (c) and W (d) in arbitrary units. The data are in black (solid) and the results of Monte Carlo simulations are in red (dotted). The areas under the curves are normalized to each other.

D. Kinematic corrections

1 Ionization energy-loss corrections were applied to
 2 protons and electrons in both data and Monte-
 3 Carlo events. These corrections were estimated using
 4 the GSIM Monte Carlo program. Due to im-
 5 perfect knowledge of the properties of the CLAS de-
 6 tector, such as the magnetic field distribution and
 7 the precise placement of the components or detec-
 8 tor materials, small empirical sector-dependent cor-
 9 rections had to be made on the momenta and an-
 10 gles of the detected electrons and protons. The cor-
 11 rections were determined by systematically study-
 12 ing the kinematics of the particles emitted from
 13 well understood kinematically-complete processes,
 14 e.g. elastic electron scattering. These corrections
 15

16 were on the order of 1%.

IV. EVENT SELECTION

A. Fiducial cuts

Certain areas of the detector acceptance were not efficient due to gaps in the DC, problematic SC panels, and inefficient zones of the CC and the EC. These areas were removed from the analysis as well as the simulation by means of geometrical cuts, which were momentum, polar angle and azimuthal angle dependent.

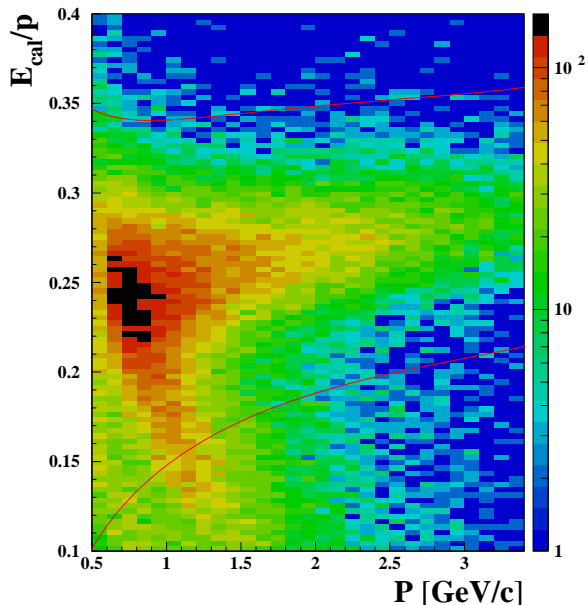


FIG. 8: (Color online). Sampling fraction E_{cal}/p of electrons in the EC as a function of electron momentum. The solid lines show the $\pm 3.5\sigma$ sampling-fraction cut used in this analysis.

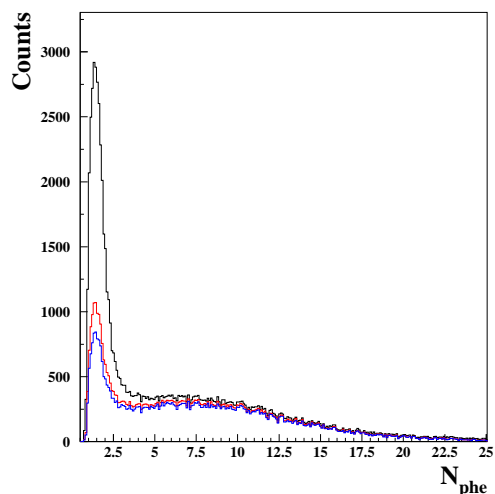
B. Exclusivity cuts

To select the exclusive reaction $ep \rightarrow e'p'\pi^0$, each event was required to contain an electron, one proton and at least two photons in the final state. Then, so called *exclusivity cuts* were applied to all combinations of an electron, a proton and two photons to ensure energy and momentum conservation, thus eliminating events in which there were any additional undetected particles.

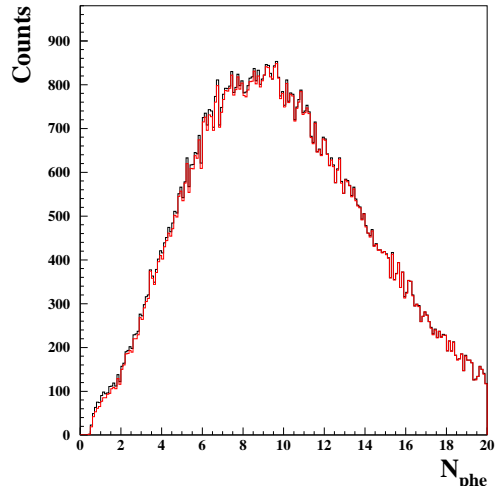
Five cuts were used for the exclusive event selection (see Fig. 11):

- A cut, θ_X , on the angle between the reconstructed π^0 momentum vector and the missing momentum vector for the reaction $ep \rightarrow e'p'X$, in which $\theta_X < 2^\circ$.
- The missing mass squared of the ep -system ($ep \rightarrow e'p'X$), with $|M_x^2(ep) - M_{\pi^0}^2| < 3\sigma$.
- The missing mass of the $e\gamma\gamma$ -system ($ep \rightarrow e'\gamma\gamma X$), with $|M_x(e\gamma\gamma) - M_p| < 3\sigma$.
- The missing energy ($ep \rightarrow e'p'\gamma\gamma X$), with $|E_x(ep\pi^0) - 0| < 3\sigma$.
- $\gamma\gamma$ invariant mass - $|M(\gamma\gamma) - M_{\pi^0}| < 3\sigma$.

Here σ is the observed experimental resolution obtained as the variance from the mean value of the distributions of each quantity. Three sets of resolutions were determined independently for each of the three photon-detection topologies (IC-IC, IC-EC, EC-EC). The effects of these cuts on the various distributions and the positions of the applied



(a)



(b)

FIG. 9: (a): The number of CC photoelectrons for events before the various cuts such as CC angle matching, EC sampling fraction and exclusivity cuts were applied. (b): The number of CC photoelectrons for events that pass all cuts.

cuts are shown in Fig. 11 for the case where both photons were detected in the IC. These distributions were generally broader than in the Monte Carlo simulations so that the cuts for the data were typically broader than those used for the Monte Carlo simulations. Similar results were obtained for the topology in which one photon was detected in the IC and one in the EC, as well as the case where both photons were detected in the EC.

C. Background subtraction

The $M(\gamma\gamma)$ distribution contains a small amount of background under the π^0 peak even after the application of all exclusivity cuts shown in Fig. 11. The background under the π^0 invariant mass peak, typ-

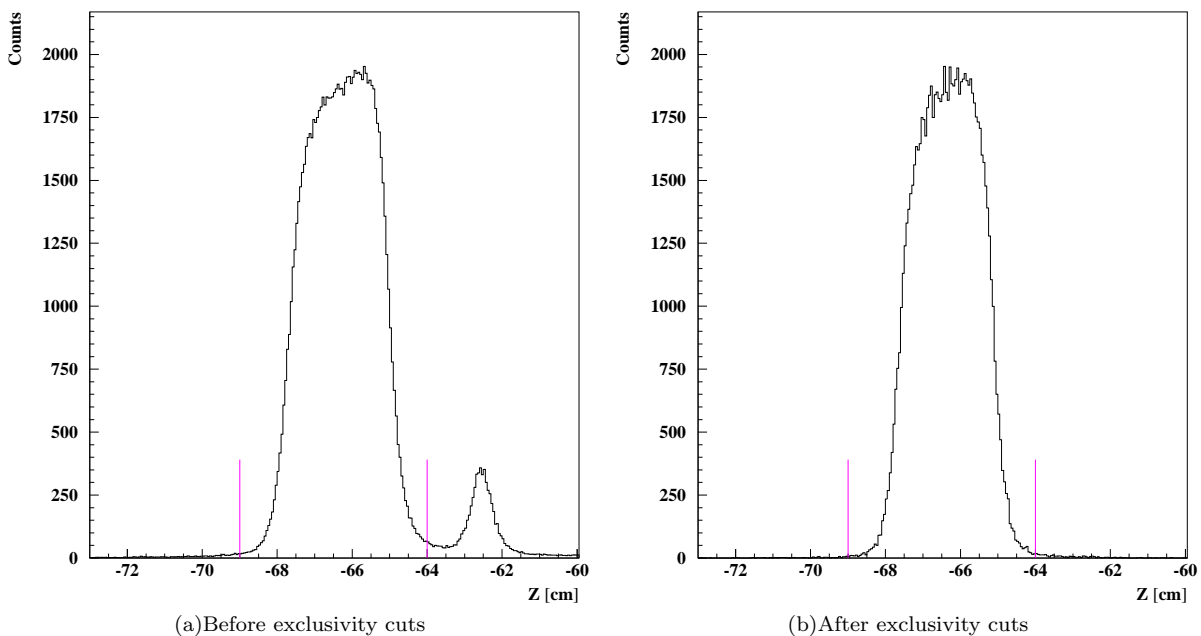


FIG. 10: The z -coordinate of the electron vertex. The vertical lines are the positions of the applied cuts. Note in (a) the small peak to the right of the target that is due to a foil placed at $z = -62.5$ cm downstream of the target window. In (b) the peak due to the foil is seen to disappear after the selection of the exclusive reaction.

1 ically 3–5%, was subtracted for each kinematic bin
 2 using the data in the sidebands $(-6\sigma, -3\sigma) \cup (3\sigma, 6\sigma)$
 3 in the $M(\gamma\gamma)$ distributions (lower right distribution
 4 in Fig. 11 and in greater detail in Fig. 12). The same
 5 cuts were applied to all the kinematic bins.

D. Kinematic binning

7 The kinematics of the reaction are defined by four
 8 variables: Q^2 , x_B , t and ϕ_π . In order to obtain
 9 differential cross sections the data were divided into
 10 four-dimensional rectangular bins in these variables.
 11 There are 8 bins in x_B , Q^2 and t as shown in Tables
 12 I–III. For each of these kinematic bins there are 20
 13 bins in ϕ_π of equal angular width. The binning in
 14 x_B and Q^2 is shown in Fig. 6.

V. MONTE CARLO SIMULATION

16 The acceptance for each (Q^2, x_B, t, ϕ_π) bin of the
 17 CLAS detector with the present setup for the reac-
 18 tion $ep \rightarrow e'p'\gamma\gamma$ was calculated using the Monte
 19 Carlo program GSIM. The event generator used an
 20 empirical parametrization of the cross section as a
 21 function of Q^2 , x_B and t . The parameters were
 22 tuned using the MINUIT program to best match
 23 the simulated π^0 cross section with the measured
 24 electroproduction cross section. Two iterations were
 25 found to be sufficient to describe the experimental
 26 cross section and distributions. The comparisons of
 27 the experimental and Monte Carlo simulated distri-

TABLE I: Q^2 bins

Bin Number	Lower Limit (GeV ²)	Upper limit (GeV ²)
1	1.0	1.5
2	1.5	2.0
3	2.0	2.5
4	2.5	3.0
5	3.0	3.5
6	3.5	4.0
7	4.0	4.6

TABLE II: x_B bins

Bin Number	Lower Limit	Upper limit
1	0.10	0.15
2	0.15	0.20
3	0.20	0.25
4	0.25	0.30
5	0.30	0.38
6	0.38	0.48
7	0.48	0.58

TABLE III: $|t|$ bins

Bin Number	Lower Limit (GeV ²)	Upper limit (GeV ²)
1	0.09	0.15
2	0.15	0.20
3	0.20	0.30
4	0.30	0.40
5	0.40	0.60
6	0.60	1.00
7	1.00	1.50
8	1.50	2.00

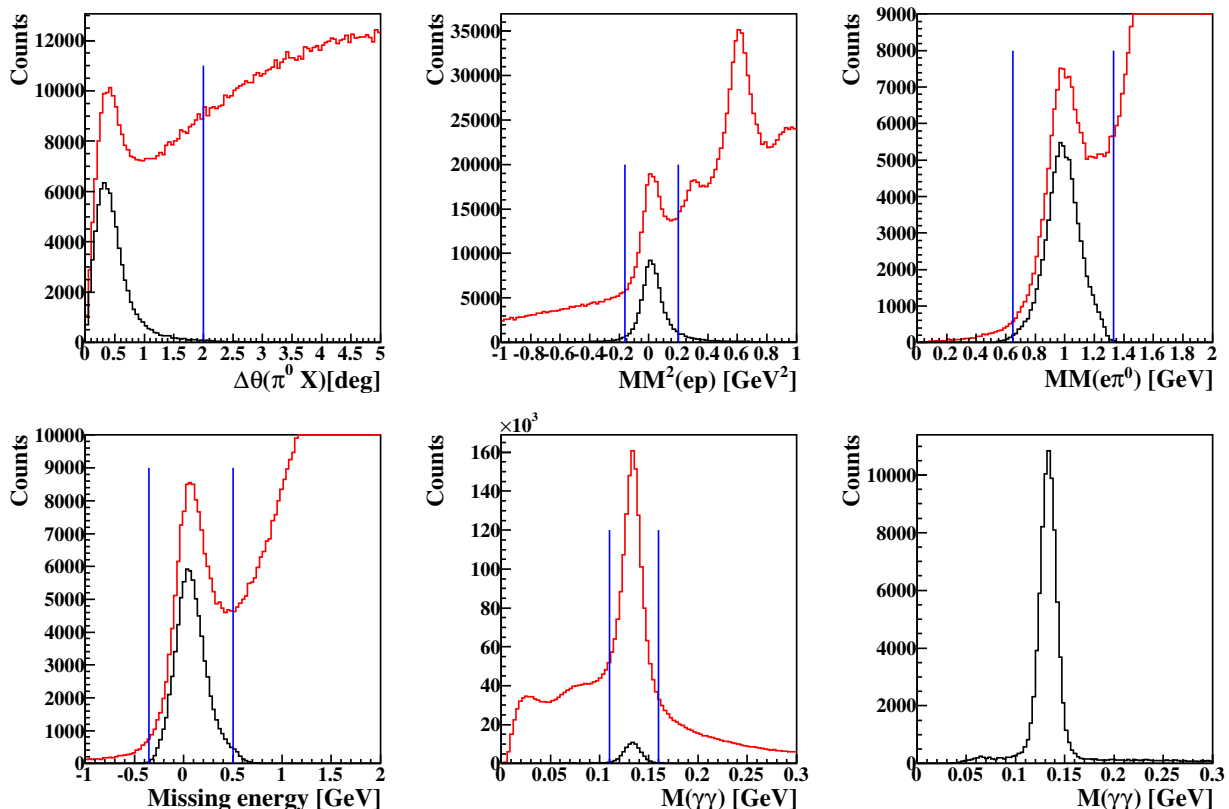


FIG. 11: (Color online) The exclusivity cuts for π^0 production for the topology where both decay photons are detected in the IC calorimeter. The graph for each variable shows the number of events per channel plotted before (red) and after (black) the cuts on the other variables. Upper left: θ_X cut: angle between the reconstructed π^0 momentum vector and the missing momentum vector $ep \rightarrow e'p'X$. Upper middle: Missing mass $M_X^2(ep)$. Upper right: Missing mass $M_X(e\gamma)$. Lower left: Missing energy $E_X(ep\gamma\gamma)$. Lower middle: Invariant mass $M(\gamma\gamma)$. Lower right: Same as in lower middle ($M(\gamma\gamma)$), but magnified to illustrate the residual background. This background is subtracted from the pion distribution using the wings on either side of the peak, as explained in the text. The vertical lines denote the positions of the applied cuts on each distribution.

1 butions are shown in Fig. 7 for the variables Q^2 , x_B , 22
 2 $-t$ and W .

3 Additional smearing factors for tracking and tim- 24
 4 ing resolutions were included in the simulations to 25
 5 provide more realistic resolutions for charged parti- 26
 6 cles. The Monte Carlo events were analyzed by the 27
 7 same code that was used to analyze the experimental 28
 8 data, and with the additional smearing and some- 29
 9 what different exclusivity cuts, to account for the 30
 10 leftover discrepancies in calorimeter resolutions. Ul- 31
 11 timately the number of reconstructed Monte Carlo 32
 12 events was an order of magnitude higher than the 29
 13 number of reconstructed experimental events. Thus, 30
 14 the statistical uncertainty introduced by the accep- 31
 15 tance calculation was typically much smaller than 32
 16 the statistical uncertainty of the data.

17 The efficiency of the event reconstruction depends 33
 18 on the level of noise in the detector, the greater the 34
 19 noise the lower the efficiency. It was found that the 35
 20 efficiency for reconstructing particles decreased lin- 34
 21 early with increasing beam current. To take this 35

into account the background hits from random 3- 23
 Hz-trigger events were mixed with the Monte Carlo 24
 events for all detectors - DC, EC, IC, SC and CC. 25
 The acceptance for a given bin i was calculated as 26
 a ratio of the number of reconstructed events to the 27
 number of generated events, including the random 28
 background events as

$$\epsilon_i(Q^2, x_B, t, \phi_\pi) = \frac{N_i^{rec}(Q^2, x_B, t, \phi_\pi)}{N_i^{gen}(Q^2, x_B, t, \phi_\pi)}. \quad (1)$$

Only areas of the 4-dimensional space with an accep-
 tance equal to or greater than 0.5% were used.
 This cut was applied to avoid the regions where the
 calculation of the acceptance was not reliable.

VI. RADIATIVE CORRECTIONS

Radiative processes which modify the observed
 cross section were taken into account. Some of these,

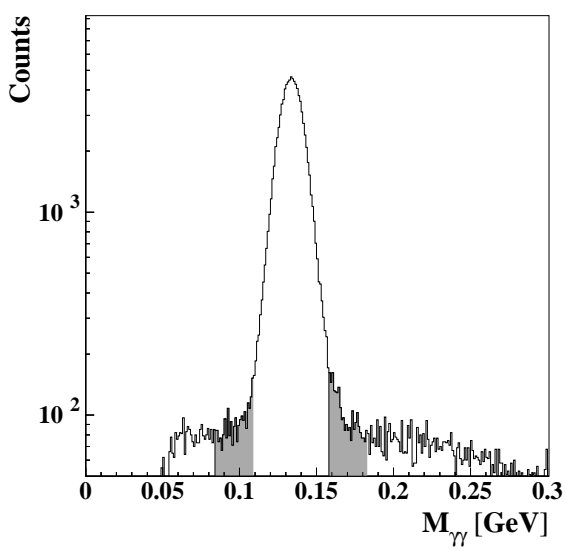


FIG. 12: The invariant mass distribution $M(\gamma\gamma)$ for all events in which all selection criteria were applied, where both decay photons were detected in the IC (note the log scale). The shaded regions were used to estimate the residual background on a kinematic bin-by-bin basis.

illustrated in Fig. 13, include radiation of real photons, vacuum polarization and lepton-photon vertex corrections. Vacuum polarization refers to the process where the virtual photon temporarily creates and annihilates a lepton-anti-lepton pair. The lepton-photon vertex corrections are for processes where a photon is emitted by the incoming electron and is absorbed by the outgoing electron. These processes give the largest contribution to the cross section at the next-to-leading-order level and can be calculated exactly from QED [26]. Thus, the measured cross section can be corrected to extract the Born term. The radiative correction, δ_{RC} , connects the experimentally measured cross section to the basic non-radiative (Born) cross section as follows

$$\sigma_{Born} = \frac{\sigma_{meas}}{\delta_{RC}}. \quad (2)$$

Here, σ_{meas} is the observed cross section from experiment and σ_{Born} is the desired cross section after corrections.

The corrections were obtained using the software package EXCLURAD [26] which uses theoretical models as input for the hadronic current. The same analytical structure functions were implemented in the EXCLURAD package as were used to generate the π^0 electroproduction events in the Monte-Carlo simulation. The corrections were computed for each kinematic bin (Q^2, x_B, t, ϕ_π). They vary from 5% to 10%, depending on the kinematics. For example, Figure 14 shows the radiative corrections calculated for the first kinematic bin as a function of the ϕ_π angle. Note that the correction increases near $\phi_\pi = 0^\circ$ and $\phi_\pi = 360^\circ$.

VII. NORMALIZATION CORRECTION

To check the overall absolute normalization the cross section of elastic electron-proton scattering was measured using the same data set. The measured cross section was lower than the known elastic cross section by approximately 12% over most of the elastic kinematic range. Studies made using additional other reactions where the cross sections are well known, such as π^0 production in the resonance region, and Monte Carlo simulations of the effects of random backgrounds, indicate that this was approximately true over a wide range of kinematics. Thus, a normalization factor $\delta_{Norm} \sim 0.89$ was applied to the measured cross section. This value includes the efficiency of the SC counters which was estimated to be around around 95%, as well as other efficiency factors which are not accounted for in the analysis, such as trigger and CC efficiency effects. This correction comprises the largest single contribution to the systematic uncertainties in the extracted cross section.

VIII. SYSTEMATIC UNCERTAINTIES

The determination of the differential cross section of the reaction $ep \rightarrow e'p'\pi^0$ requires the knowledge of the yield and the acceptance, including various efficiency factors and radiative effects, for each kinematic bin (Q^2, x_B, t, ϕ_π), as well as the integrated luminosity of the experiment. These quantities are subject to systematic uncertainties which contribute to the uncertainty of the measured cross section in each kinematic bin. Each of these factors is subject to systematic uncertainty. The size of these systematic uncertainties was estimated by repeating the calculation of the cross section varying each of the cut parameters within reasonable limits. Table IV contains a summary of the information on all the studied sources of systematic uncertainties. Some sources of uncertainty vary bin-by-bin, others are global.

The systematic uncertainty on the proton identification was studied by removing the cut on the difference between the measured and predicted flight times. The systematic uncertainty was estimated in each (Q^2, x_B, t, ϕ_π) bin to be on average $\sim 2.5\%$.

To estimate the systematic uncertainty introduced by the electron and proton fiducial cuts, we varied the cuts applied to the ϕ angles accepted in each sector. The ϕ acceptance of each of the six sectors was less than 60° , depending on θ , due to the thickness of the toroid magnet coil cryostats. In order to avoid tracks which are too close to the coils, a fiducial cut in $\Delta\phi$ was applied of nominally 40° ($\pm 20^\circ$ from the sector mid-plane) at larger angles θ , tapering down to smaller $\Delta\phi$ for smaller θ as the ϕ acceptance decreases. For electrons an additional cut of $\pm 3^\circ$ from the mid-plane was applied to avoid known

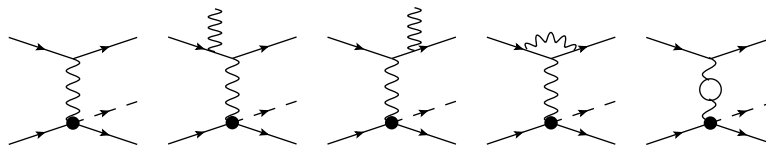


FIG. 13: Feynman diagrams contributing to the pion electroproduction cross section. Left to right: Born process, Bremsstrahlung (by the initial and the final electron), vertex correction, and vacuum polarization.

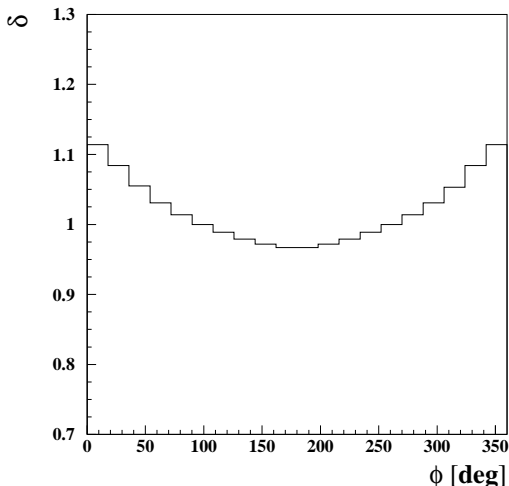


FIG. 14: Radiative corrections for π^0 electroproduction as a function of ϕ_π for the bin ($Q^2 = 1.25 \text{ GeV}^2$, $x_B = 0.125$, $t = -0.12 \text{ GeV}^2$).

1 inefficiencies of the Cherenkov detector in the sector 39
2 mid-plane. The average systematic uncertainty arising 40
3 from the placement of these cuts was estimated 41
4 to be around 4.7%.

5 The lower limit on the photon's energy in the EC 43
6 calorimeter was varied from 350 MeV to 300 MeV for 44
7 the evaluation of the systematic uncertainties due to 45
8 this selection criteria. The uncertainties were calculated 46
9 for each bin and on average were estimated to be
10 $\sim 1.6\%$.

11 The systematic uncertainties due to the exclusiv- 47
12 ity cuts on $M_x(e\gamma\gamma)$, $E_x(ep\pi^0)$, and $M(\gamma\gamma)$ were
13 studied in detail for each cut independently. The

The four-fold differential cross section as a function of the four variables (Q^2, x_B, t, ϕ_π) was obtained from the expression

$$\frac{d^4\sigma_{ep \rightarrow e'p'\pi^0}}{dQ^2 dx_B dt d\phi_\pi} = \frac{N(Q^2, x_B, t, \phi)}{\mathcal{L}_{int}(\Delta Q^2 \Delta x_B \Delta t \Delta \phi)} \times \frac{1}{\epsilon_{ACC} \delta_{RC} \delta_{Norm} Br(\pi^0 \rightarrow \gamma\gamma)}. \quad (3)$$

48 The definitions of the kinematic variables are given 50
49 in Appendix A. The definitions of the other quanti-

14 cuts were changed from 3σ to 2σ and systematic un-
15 certainties were calculated in each bin. The average
16 uncertainties for each cut, shown in Table IV, varied
17 between 2.5–3.2%.

18 The systematic uncertainty of the radiative correc-
19 tions was estimated as follows. The missing mass
20 of the ep system $M_x(ep)$ exhibits a radiative tail.
21 Thus, when making a cut on $M_x(ep)$ there is a loss
22 of radiated events, which was corrected using the
23 routine EXCLURAD [26], which depends on the
24 value of the cut. The correction procedure was ap-
25 plied with varied cuts on $M_x(ep)$ from 0.1 GeV to
26 0.25 GeV in the data analysis program, and the same
27 value of this cut was applied to the simulated data.
28 The obtained cross sections were compared to the
29 original ones bin-by-bin. On average the uncertainty
30 was estimated to be 2.9%.

31 The systematic uncertainty in the cross section
32 due to the normalization correction factor was esti-
33 mated by the comparison of the normalization factors
34 extracted from the six independent measurements of
35 the elastic cross section in the six different CLAS
36 sectors. The absolute normalization correction reflects
37 systematic uncertainties which were not accounted for
38 and which may lead to normalization errors. This
systematic uncertainty was estimated to be 6%.

The uncertainty in the incident electron beam en-
ergy was determined to be about 0.017 GeV and its
contribution to the overall cross section is small.

Finally, the overall systematic uncertainty was es-
timated by adding all contributions in quadrature
and is about 10%.

IX. CROSS SECTIONS FOR $\gamma^*p \rightarrow \pi^0 p$

TABLE IV: Summary table of systematic uncertainties. B denotes bin-to-bin and O indicates overall uncertainties

Source	Bin-to-bin or overall	Average Uncertainty
Proton ID	B	$\sim 2.5\%$
Fiducial cut	B	$\sim 4.7\%$
Cut on energy of photon detected in the EC	B	$\sim 1.6\%$
Cut on missing mass of the $e\gamma\gamma$	B	$\sim 2.5\%$
Cut on invariant mass of 2 photons	B	$\sim 2.9\%$
Cut on missing energy of the $e\gamma\gamma$	B	$\sim 3.2\%$
Radiative corrections	B	$\sim 2.9\%$
Total beam charge on target	O	$< 1\%$
Target length	O	0.2%
Absolute normalization	O	6.0%

- 1 • $N(Q^2, x_B, t, \phi_\pi)$ is the number of $ep \rightarrow e'p'\pi^0$ 17
- 2 events in a given (Q^2, x_B, t, ϕ_π) bin; 18
- 3 • \mathcal{L}_{int} is the integrated luminosity (which takes 19
- 4 into account the correction for the data- 20
- 5 acquisition dead time); 21
- 6 • $(\Delta Q^2 \Delta x_B \Delta t \Delta \phi_\pi)$ is the corresponding bin 22
- 7 width (see Tables I–III). For bins not com- 23
- 8 pletely filled, because of cuts in θ_e , W and 24
- 9 E' , as seen in Fig. 6, the phase space 25
- 10 $(\Delta Q^2 \Delta x_B \Delta t \Delta \phi_\pi)$ includes a 4-dimensional 26
- 11 correction to take this into account. The spec- 27
- 12 ified Q^2 , x_B and t values are the mean val- 28
- 13 ues of the data for each variable for each 4- 29
- 14 dimensional bin, as if the cross sections in each 30
- 15 bin vary linearly in each variable in the filled 31
- 16 portion of the accepted kinematic volume.
- ϵ_{ACC} is the acceptance calculated for each bin (Q^2, x_B, t, ϕ_π) ;
- δ_{RC} is the correction factor due to the radiative effects calculated for each (Q^2, x_B, t, ϕ_π) bin;
- δ_{Norm} is the overall absolute normalization factor calculated from the elastic cross section measured in the same experiment (see Sec. VIII above);
- $Br(\pi^0 \rightarrow \gamma\gamma) = \frac{\Gamma(\pi^0 \rightarrow \gamma\gamma)}{\Gamma_{total}}$ is the branching ratio for the $\pi^0 \rightarrow \gamma\gamma$ decay mode.

The reduced or “virtual photon” cross sections were extracted from the data through:

$$\frac{d^2 \sigma_{\gamma^* p \rightarrow p' \pi^0}(Q^2, x_B, t, \phi_\pi, E)}{dtd\phi} = \frac{1}{\Gamma_V(Q^2, x_B, E)} \frac{d^4 \sigma_{ep \rightarrow e' p' \pi^0}}{dQ^2 dx_B dtd\phi_\pi}. \quad (4)$$

30 The Hand convention [27] was adopted for the defi- 45

31 nition of the virtual photon flux Γ_V (see Eq. B2 in 46

32 Appendix B). A table of the 1867 reduced cross sec- 47

33 tions can be obtained online in Ref. [28]. As an ex- 48

34 ample of the information available, Table V presents 49

35 the reduced cross section for one kinematical point 50

36 ($Q^2=1.15 \text{ GeV}^2$, $x_B=0.132$, $t=-0.12 \text{ GeV}^2$). 51

37 A. Integrated virtual photon cross section

$$38 \quad \sigma_U = \sigma_T + \epsilon \sigma_L$$

39 The total virtual photon cross section is defined 57

40 as the reduced differential cross section integrated 58

41 over ϕ_π and t : 59

$$42 \quad \sigma_U = \sigma_T + \epsilon \sigma_L = \int \int \frac{d^2 \sigma}{dtd\phi_\pi} dtd\phi_\pi, \quad (5)$$

43 where σ_T and σ_L are due to transverse and longitu- 60

44 dinal photons respectively. σ_U depends on two vari- 61

ables Q^2 and x_B . The variable ϵ is the ratio of fluxes

of longitudinally and transversely polarized virtual photons (see Eq. B3 in the appendix).

Since the CLAS acceptance has limited coverage in some areas of the 4-dimensional phase space (Q^2, x_B, t, ϕ_π) , the integral could be carried out over a finite range of the total phase space. For example, at high Q^2 and x_B , the acceptance around $\phi_\pi = 180^\circ$ is near zero, so the ϕ_π integral cannot be fully calculated using the present data. To account for regions with small acceptance, a model that was developed for the Monte Carlo generator to describe $d^2 \sigma^{MC}/dtd\phi_\pi$ was used. This generator was tuned using our own π^0 experimental data. Thus the integrated cross sections have an additional factor $1/\eta$, where

$$62 \quad \eta = \frac{\int \int_{\Omega'} \frac{d^2 \sigma^{MC}}{dtd\phi_\pi} dtd\phi_\pi}{\int \int_{\Omega} \frac{d^2 \sigma^{MC}}{dtd\phi_\pi} dtd\phi_\pi}, \quad (6)$$

in which Ω is the full phase space and Ω' is the phase space where CLAS has non-zero acceptance. Only

TABLE V: $d^2\sigma/dtd\phi_\pi$ at $t = -0.18$ GeV², $x_B = 0.22$ and $Q^2 = 1.75$ GeV². The complete numerical listing for all measured kinematic points is found in Ref. [28].

ϕ_π (deg)	$\frac{d^2\sigma}{dt d\phi_\pi}$ (nb/GeV ²)	Statistical Error (nb/GeV ²)	Systematic Error (nb/GeV ²)
9	55.8	9.0	12.0
27	45.5	6.1	0.7
45	56.7	5.9	6.0
63	62.0	6.3	6.6
81	70.8	6.1	11.1
99	85.2	6.5	7.0
117	61.7	6.4	5.8
135	41.2	5.9	4.6
153	35.7	5.5	3.6
171	44.8	7.8	0.5
189	30.9	5.9	3.6
207	41.0	5.9	5.6
225	42.9	6.5	2.8
243	51.8	5.8	8.8
261	69.2	6.0	2.4
279	82.3	7.3	3.6
297	77.5	7.1	4.2
315	57.8	5.5	9.8
333	48.7	6.2	4.4
351	37.3	7.8	8.2

TABLE VI: Parameters of Q^2 -dependent fits to the t -integrated cross sections in Fig. 15 for different values of x_B .

x_B	A_{Q^2}	n
0.18	0.38 ± 0.16	3.32 ± 2.04
0.22	0.97 ± 0.39	5.26 ± 1.34
0.28	1.11 ± 0.48	4.09 ± 1.12
0.34	2.06 ± 0.71	4.46 ± 0.77
0.43	5.41 ± 1.83	5.22 ± 0.63
0.51	5.19 ± 3.12	4.39 ± 0.91

1 data points were included for partially covered kinematic volumes in which η was greater than 0.45 to avoid extrapolation to the regions where the acceptance is low. The value of η is model dependent, which introduces an additional systematic uncertainty of $\sim 15\%$. The integration over the variable $|t|$ extends from $|t_{min}|$ to 2 GeV².

2 The results have been found to be consistent with the results of Ref. [14], which reported high accuracy cross sections near the lower Q^2 , W and $|t|$ regions of the present experiment.

3 Fig. 15 shows the integrated cross section σ_U as a function of Q^2 for different values of x_B . The cross sections were fit by the simple expression $\sigma_U \sim 1/Q^n$ to estimate the Q^2 dependence. The weighted mean of the exponent parameters is $n = 4.7 \pm 0.7$. Reference [14] finds $n = 4.78 \pm 0.16$ based upon two values of Q^2 (1.9 and 2.3 GeV²). The asymptotic prediction of the conventional GPD models is $\sigma_L \sim 1/Q^6$ and $\sigma_T \sim 1/Q^8$. The parameters of the fit are given in Table VI.

4 The total cross section $\sigma_U = \sigma_T + \epsilon\sigma_L$ as a function of W for different values of Q^2 is shown in Fig. 16. The cross sections were fitted with the function $\sigma \sim 1/W^n$. The weighted mean value of the exponent is $n = 3.7 \pm 0.3$. Ref. [14] finds $n = 3.48 \pm 0.11$ based upon two values of W . The W dependence is

TABLE VII: Parameters of W -dependent fits to the t -integrated cross sections in Fig. 16 for different values of Q^2 .

Q^2	A_W	n
1.34	5.01 ± 2.94	3.03 ± 0.56
1.79	7.82 ± 2.77	3.64 ± 0.37
2.22	11.90 ± 3.53	4.23 ± 0.33
2.68	5.76 ± 2.64	3.61 ± 0.52
3.21	2.38 ± 1.56	2.68 ± 0.80
3.71	1.30 ± 1.24	2.12 ± 1.20

28 consistent with what was observed for ρ electroproduction [29], i.e. the cross section decreases with W compatibly with the Regge-model predictions [20] for the exclusive reactions. The parameters of the fit are given in Table VII.

B. The t -dependent differential cross section

$$d\sigma_U/dt$$

Integrating only over ϕ_π yields the t -dependent differential cross section

$$\frac{d\sigma_U}{dt} = \int \frac{d^2\sigma}{dt d\phi_\pi} d\phi_\pi. \quad (7)$$

The correction factor for the region where the CLAS detector has zero acceptance was calculated as

$$\eta' = \frac{\int_{\Omega^*} \frac{d^2\sigma}{dt d\phi_\pi}^{MC} d\phi_\pi}{\int_{\Omega} \frac{d^2\sigma}{dt d\phi_\pi}^{MC} d\phi_\pi}, \quad (8)$$

in which Ω is the full phase space and Ω^* is the phase space where CLAS has non-zero acceptance.

Fig. 17 shows the cross section $d\sigma_T/dt + \epsilon d\sigma_L/dt$ for intervals of Q^2 for the different values of x_B . The presented cross sections were calculated only for the kinematics where the factor η' was greater than 0.45. The general feature of these distributions is that in a small interval near $|t| = |t_{min}|$ they are not diffractive. There, the cross sections cannot be described by simple exponential functions. However, for somewhat larger values of $|t|$, the cross sections appear to fall off exponentially with $-t$, and thus were fit by the function e^{bt} , where the exponential functions appears to fit the data with a good χ^2 . This provides a qualitative description of the $|t|$ -dependence by a slope parameter b . The curves in Fig. 17 are the results of these fits.

Fig. 18 shows the slope parameter b as a function of x_B for different values of Q^2 . The values of b are between 1 and 2.5 GeV⁻². The data appear to exhibit a slope parameter decrease with increasing x_B for each Q^2 over much of the measured range, except at the highest measured regions of x_B and Q^2 . However, the Q^2 - x_B correlation in the CLAS acceptance does not permit one to make a definite conclusion about the Q^2 dependences of the slope parameter for

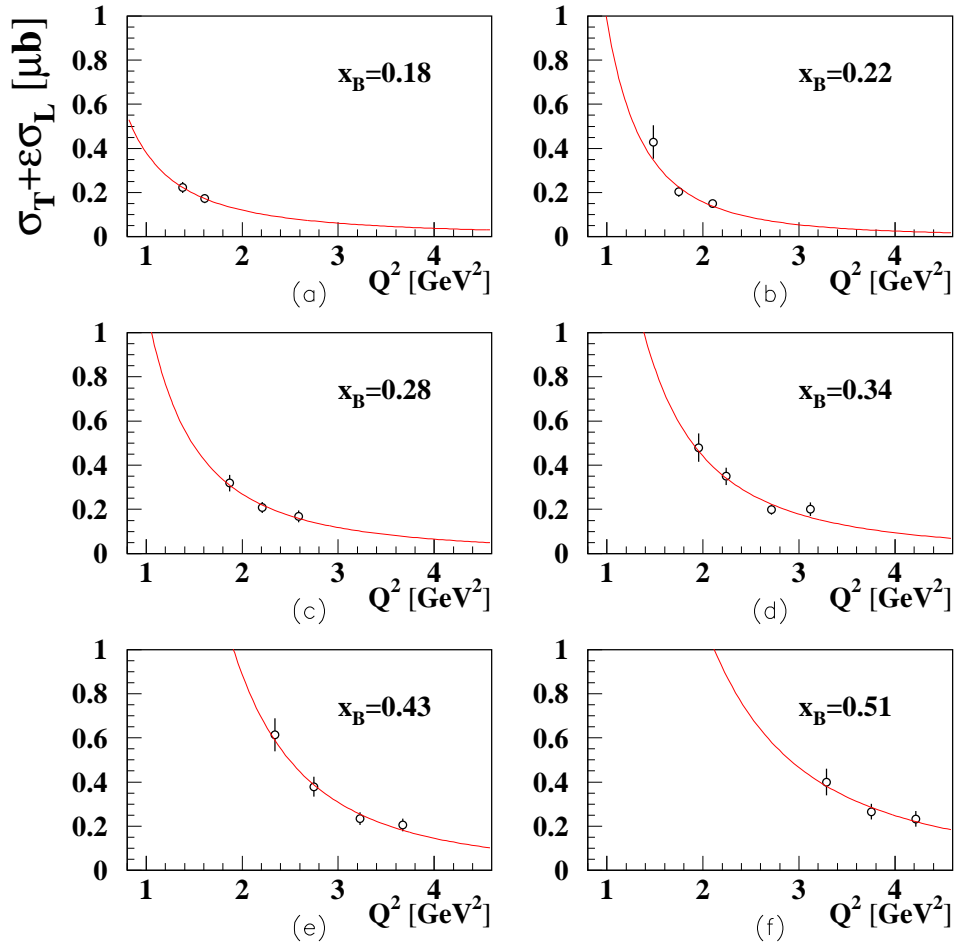


FIG. 15: (color online) The t -integrated “virtual photon” cross section $\sigma_T + \epsilon\sigma_L$ as a function of Q^2 for the reaction $\gamma^*p \rightarrow p'\pi^0$ for $x_B=0.18, 0.22, 0.28, 0.34, 0.43$ and 0.51 . The curves are fits to a power law $\sigma_U = A_{Q^2}/Q^n$ where A_{Q^2} and n are fit parameters.

1 fixed x_B . What one can say is that at high Q^2 and
 2 high x_B ($Q^2 = 4.3 \text{ GeV}^2$, $x_B=0.53$), the slope pa-
 3 rameter is smaller than for the lowest values of these
 4 variables ($Q^2 = 1.2 \text{ GeV}^2$, $x_B=0.12$). The b param-
 5 eter in the exponential determines the width of the
 6 transverse momentum distribution of the emerging
 7 protons, which, by a Fourier transform, is inversely
 8 related to the transverse size of the interaction re-
 9 gion from which the proton emerges. From the point
 10 of view of the handbag picture, it is inversely related
 11 to the separation, r_\perp , between the active quark and
 12 the center of momentum of the spectators (see Ref. 19

[30]). Thus the data implies that the separation is
 larger at the lowest x_B and Q^2 and becomes smaller
 for increasing x_B and Q^2 , as it must.

C. Structure functions

The reduced cross sections can be expanded
 in terms of structure functions $d\sigma_T/dt$, $d\sigma_L/dt$,
 $d\sigma_{LT}/dt$, and $d\sigma_{TT}/dt$ as follows:

$$\frac{d^2\sigma}{dt d\phi_\pi} = \frac{1}{2\pi} \left[\left(\frac{d\sigma_T}{dt} + \epsilon \frac{d\sigma_L}{dt} \right) + \epsilon \cos 2\phi_\pi \frac{d\sigma_{TT}}{dt} + \sqrt{2\epsilon(1+\epsilon)} \cos \phi_\pi \frac{d\sigma_{LT}}{dt} \right], \quad (9)$$

20 from which the three combinations of structure func-
 21 tions, $(\frac{d\sigma_T}{dt} + \epsilon \frac{d\sigma_L}{dt})$, $\frac{d\sigma_{TT}}{dt}$ and $\frac{d\sigma_{LT}}{dt}$ can be extracted

by fitting the cross sections to the ϕ_π distribution in

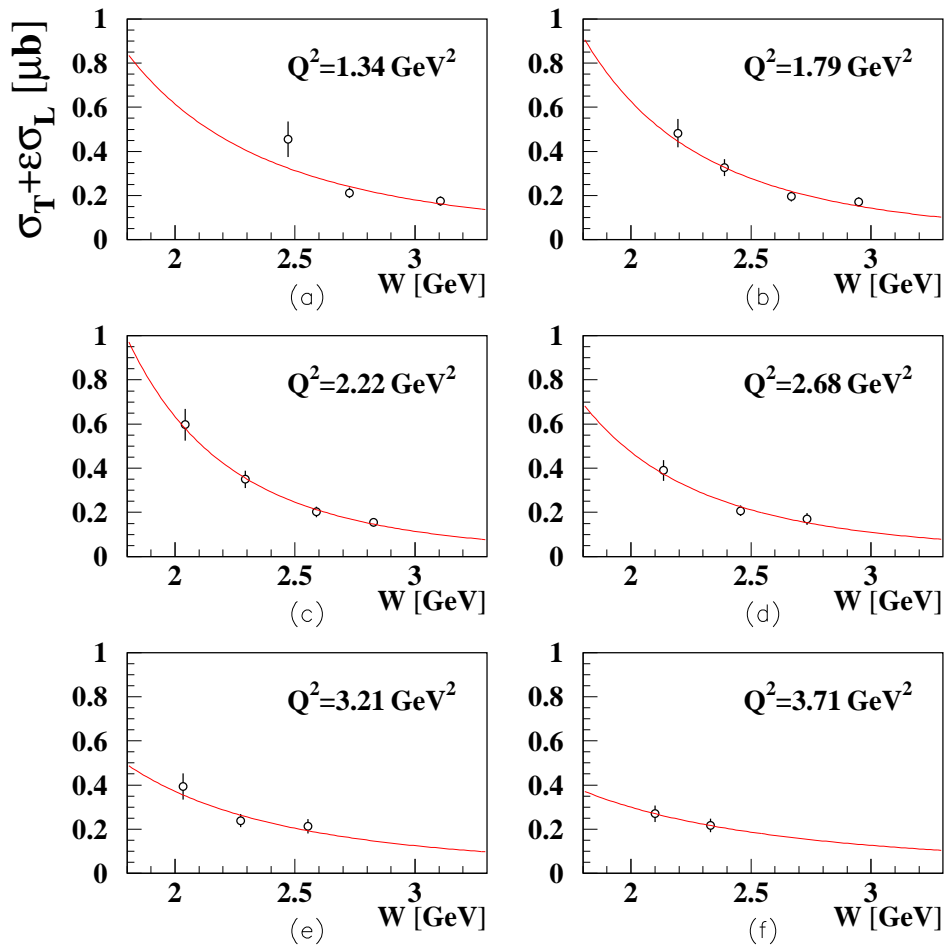


FIG. 16: (Color online) The t -integrated “virtual photon” cross section $\sigma_T + \epsilon\sigma_L$ as a function of W for the reaction $\gamma^*p \rightarrow p'\pi^0$ for $Q^2=1.34, 1.79, 2.22, 2.68, 3.21$ and 3.71 GeV^2 . The curves are fits to a power law $\sigma_U = A_W/W^n$ where A_W and n are fit parameters.

1 each bin of (Q^2, x_B, t) . The decomposition of the
 2 structure functions in terms of helicity amplitudes
 3 is given in Appendix B, Eqs. B10 to B13.

4 The physical significance of the structure func-
 5 tions is as follows:

- 6 - $d\sigma_L/dt$ is the sum of structure functions initiated
 7 by a longitudinal virtual photon, both
 8 with and without nucleon helicity-flip, i.e. res-
 9 pectively $\Delta\nu = \pm 1$ and $\Delta\nu = 0$.
- 10 - $d\sigma_T/dt$ is the sum of structure functions which
 11 are initiated by a transverse virtual photon of
 12 positive and negative helicity ($\mu = \pm 1$), with
 13 and without nucleon helicity flip, respectively
 14 $\Delta\nu = \pm 1$ and 0.
- 15 - $d\sigma_{LT}/dt$ corresponds to interferences involving
 16 products of amplitudes for longitudinal and
 17 transverse photons.
- 18 - $d\sigma_{TT}/dt$ corresponds to interferences involving
 19 products of transverse positive and negative
 20 photon helicity amplitudes.

Figure 19 shows a typical ϕ_π -distribution of the
 virtual photon cross sections with a fit using the
 form of Eq. 9. These data are listed in Table V as
 well. The complete listing of all differential cross sec-
 tions for all kinematic settings are found in Ref. [28].

Fig. 20 shows the extracted structure functions for
 all kinematical bins in (Q^2, x_B, t) . The values of the
 structure functions are given numerically in Table C.
 The results of a Regge-based calculation [20] are also
 shown in Fig. 20.

A number of observations can be made independ-
 ently of the model predictions. The $d\sigma_{TT}/dt$ struc-
 ture function is negative and $|d\sigma_{TT}/dt|$ is compa-
 rable in magnitude with the unpolarized structure
 function ($d\sigma_T/dt + \epsilon d\sigma_L/dt$). However, $d\sigma_{LT}/dt$
 is small in comparison with $d\sigma_U/dt$ and $d\sigma_{TT}/dt$.
 This reinforces the conclusion that the asymptotic
 leading-order handbag approach for which $d\sigma_L/dt$ is
 dominant is not applicable at the present values of
 Q^2 .

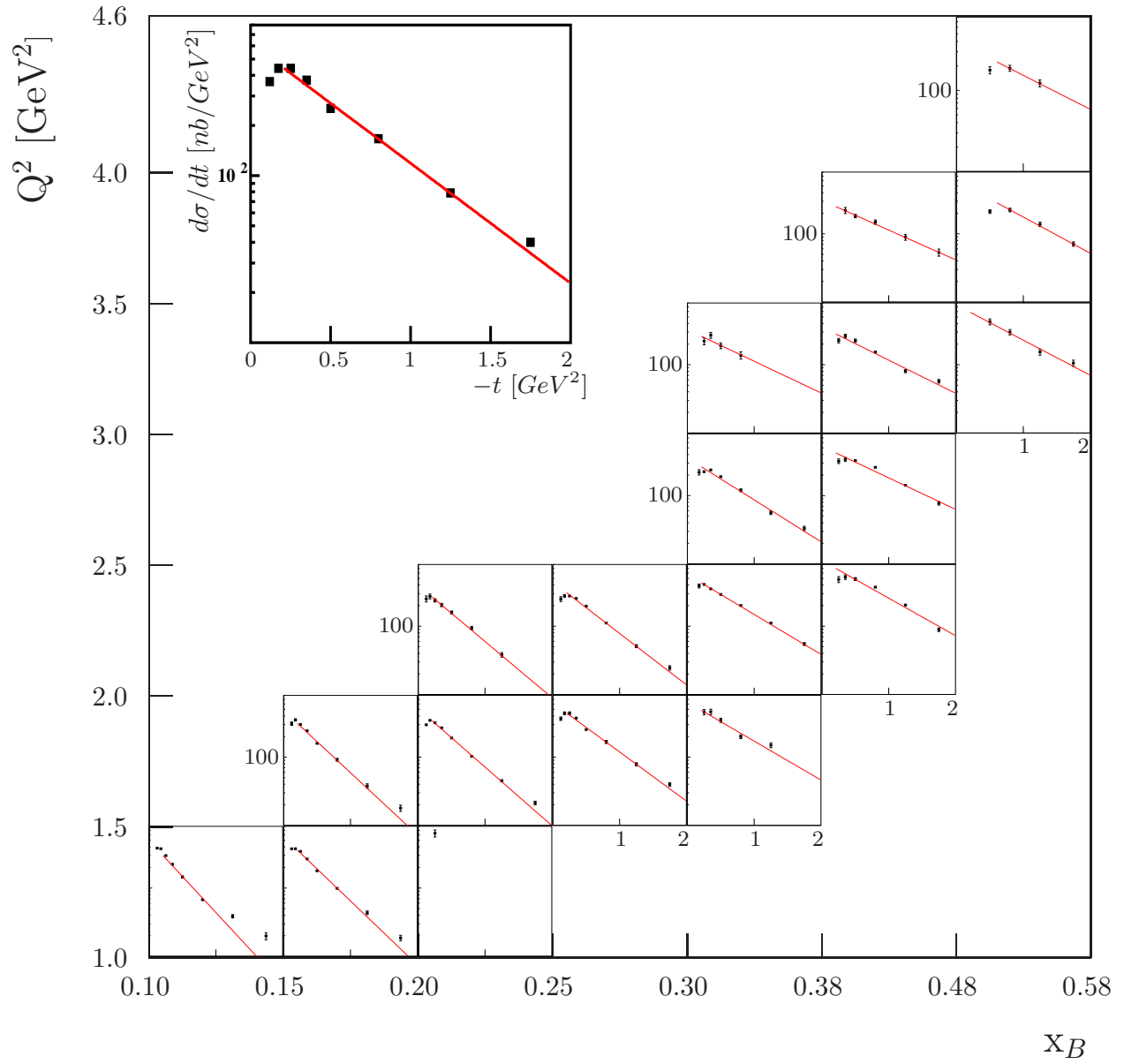


FIG. 17: (Color online) The differential cross section $d\sigma_U/dt=d\sigma_T/dt + \epsilon d\sigma_L/dt$ for the reaction $\gamma^*p \rightarrow p'\pi^0$. The curves are fits to the exponential function e^{bt} . The insert is an enlarged copy of the panel centered at $Q^2=1.75$ GeV² and $x_B=0.275$. Systematic uncertainties, including the estimated systematic uncertainty in the integration correction factor η of 15%, as discussed in the text, are not shown.

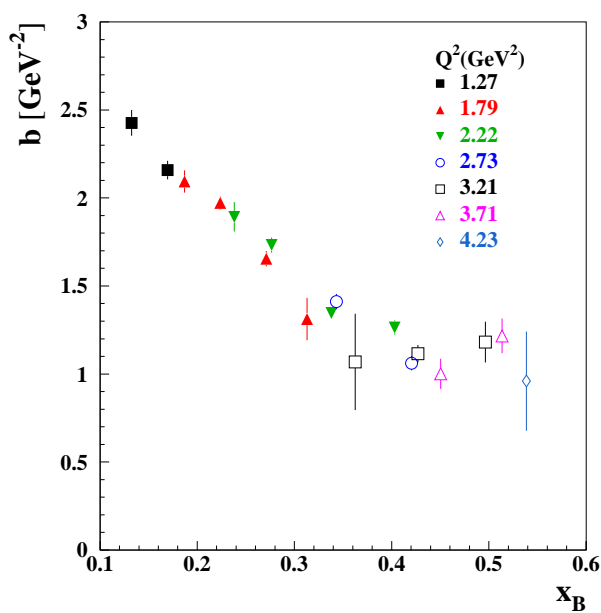


FIG. 18: (Color online) t -slope parameter b for the reaction $\gamma^*p \rightarrow p'\pi^0$ as a function of x_B for different values of Q^2 .

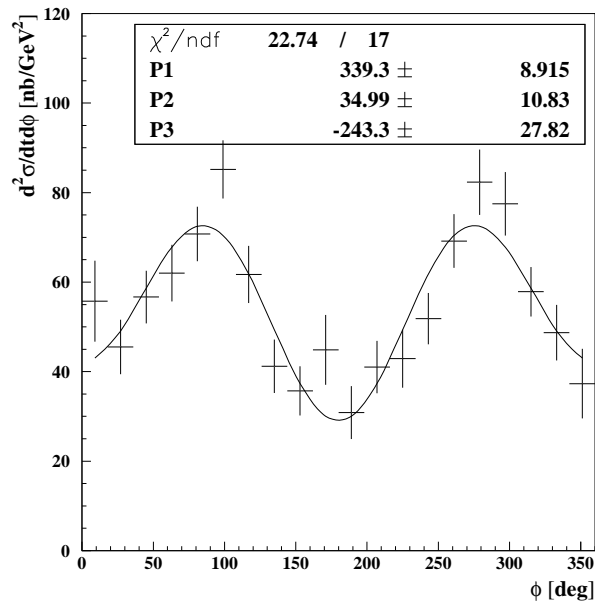


FIG. 19: Example of the ϕ_π distribution of $d^2\sigma/dtd\phi_\pi$. The solid curve is a fit of the function in Eq. 9. The kinematic bin corresponding to this figure is at $t = -0.18$ GeV^2 , $x_B = 0.22$ and $Q^2 = 1.75$ GeV^2 and the data is listed in Table V. Error bars are statistical. The complete listing of all differential cross sections for all kinematic settings are found in Ref. [28].

X. COMPARISONS WITH THEORETICAL MODELS

A. Regge model

The Regge model with charge exchange and π^\pm final state interactions, in addition to pole terms and elastic π^0 rescattering, had been successfully applied in Refs. [31, 32] to π^0 electroproduction at DESY at $Q^2 = 0.25, 0.50$ and 0.85 GeV^2 . This mechanism, which is illustrated schematically in Fig. 21, includes a charged-pion rescattering amplitude (see Fig. 22). Schematically, the amplitude can be written as a product of two terms:

$$T_{\pi N} \propto \int d\Omega T_{\gamma p \rightarrow \pi^+ N}(t_\gamma) T_{\pi N \rightarrow \pi^0 p}(t_\pi),$$

in which $t_\gamma = (k_\gamma - P_\pi)^2$. The first term in the integral is the amplitude for production of a charged off-shell meson by a virtual photon and the second characterizes its rescattering. The amplitudes are largest where the intermediate mesons become on-shell.

However, when this scheme was applied to the Jefferson Lab Hall A kinematics [14] at $Q^2 = 2.35$ GeV^2 , the calculated cross sections were found to be an order of magnitude too low (see Ref. [20]). In fact, it was very difficult to understand why the experimental cross section at $Q^2 = 2.35$ GeV^2 is comparable in magnitude to the cross section at much lower Q^2 values.

Then, Ref. [20] included a vector-meson rescattering amplitude (see Fig. 22) taking the form

$$T_{VN} \propto \int d\Omega T_{\gamma p \rightarrow VN}(t_\gamma) T_{VN \rightarrow \pi^0 p}(t_\pi).$$

It was found that the contributions of the $\rho^+\Delta^0$ and $\rho^-\Delta^{++}$ rescattering (Fig. 22 lower-right) are the most important, far more important than the ωp or $\rho^0 p$ terms because the cross section of the $N(\rho^+, \pi)N$ reaction is larger than the $N(\omega, \pi)N$ cross section, and $N(\rho^0, \pi^0)N$ cannot occur. These comparisons were only carried out in a narrow range of kinematics corresponding to the available Hall A data.

The comparison of the present data with the predictions of the Regge model [20] is shown in Fig. 20. Although the Regge model managed to describe the Hall A cross-section data in a narrow region of Q^2 and t , the situation here, with the large kinematic acceptance, is much more complex. In some regions of Q^2 and t the predictions appear better than in others. This model does predict the correct signs and values of σ_{TT} and the small value of σ_{LT} in almost all the data intervals.

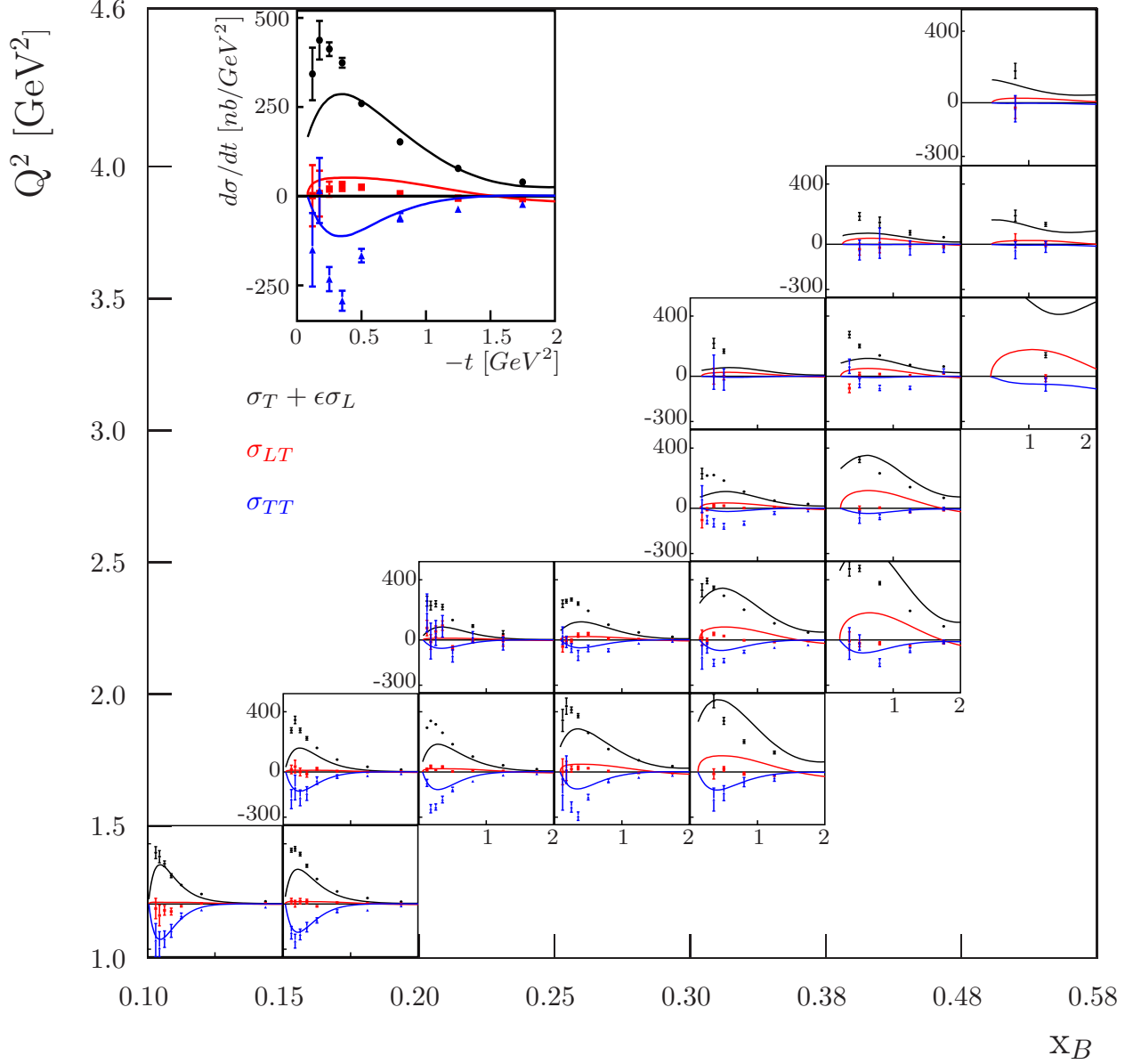


FIG. 20: (Color online) Structure functions $d\sigma_U = d\sigma_T/dt + \epsilon d\sigma_L/dt$ (black circles), $d\sigma_{TT}/dt$ (blue triangles) and $d\sigma_{LT}/dt$ (red squares) as a function of $-t$ for different Q^2 and x_B for the reaction $\gamma^* p \rightarrow p' \pi^0$. All the structure functions are numerically given in Appendix C. The error bars are statistical only. The point-by-point propagated systematic uncertainties for all the structure functions are given in Appendix C. The curves are the results of a Regge-based calculation [20]: black (positive)- $d\sigma_U/dt$, blue (negative)- $d\sigma_{TT}/dt$, and red (small)- $d\sigma_{LT}/dt$. Note that in the higher- x_B /lower- Q^2 bins that the black curves ($d\sigma_U$) from the model are much higher than the data and become off-scale.

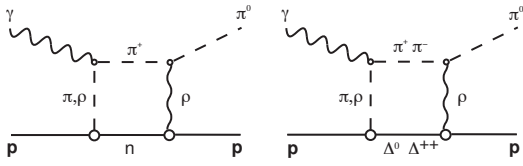


FIG. 21: Rescattering diagrams with the pion charge-exchange processes included in Ref. [20]. The vertical dashed and wavy lines represent the exchange of Regge trajectories. The horizontal lines correspond to on-shell meson nucleon rescattering processes.

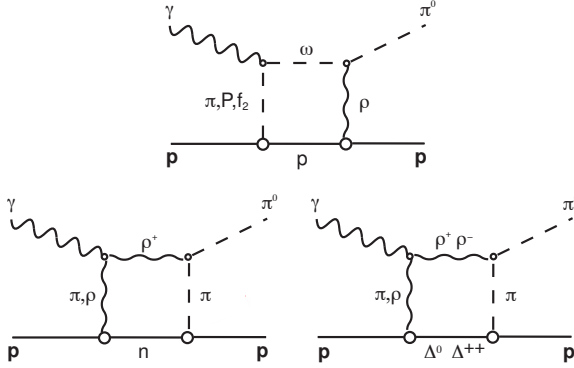


FIG. 22: Rescattering diagrams with vector meson processes included in Ref. [20].

B. Handbag model

Fig. 23 shows the experimental structure functions at selected values of Q^2 and x_B . The results of two GPD-based models which include transversity GPDs [19, 33] are superimposed in Fig. 23. The primary contributing GPDs in meson production for transverse photons are H_T , which characterizes the quark distributions involved in nucleon helicity-flip, and $\bar{E}_T (= 2\tilde{H}_T + E_T)$ which characterizes the quark distributions involved in nucleon helicity-non-flip processes [34, 35]. As a reminder, in both cases the active quark undergoes a helicity-flip.

Reference [33] obtains the following relations (see the Appendix for more details):

$$\frac{d\sigma_T}{dt} = \frac{4\pi\alpha}{2k'} \frac{\mu_\pi^2}{Q^8} \left[(1 - \xi^2) |\langle H_T \rangle|^2 - \frac{t'}{8m^2} |\langle \bar{E}_T \rangle|^2 \right] \quad (10)$$

$$\frac{d\sigma_{TT}}{dt} = \frac{4\pi\alpha}{k'} \frac{\mu_\pi^2}{Q^8} \frac{t'}{16m^2} |\langle \bar{E}_T \rangle|^2. \quad (11)$$

Here $\kappa'(Q^2, x_B)$ is a phase space factor, $t' = t - t_{min}$, where $|t_{min}|$ is the minimum value of $|t|$ corresponding to $\theta_\pi = 0$, and the brackets $\langle H_T \rangle$ and $\langle \bar{E}_T \rangle$ denote the convolution of the elementary process with the GPDs H_T and \bar{E}_T . The GPD \bar{E}_T describes the

spatial density of transversely polarized quarks in an unpolarized nucleon [34, 35].

Note that for the case of nucleon helicity-non-flip, characterized by the GPD \bar{E}_T , overall helicity from the initial to the final state is not conserved. However, angular momentum is conserved, the difference being absorbed by the orbital motion of the scattered $\pi^0 - N$ pair. This accounts for the additional $t' (= t - t_{min})$ factor multiplying the \bar{E}_T terms in Eqs. 10 and 11.

In both calculations the contribution of σ_L accounts for only a small fraction (typically less than a few percent) of the unseparated structure functions $d\sigma_T/dt + \epsilon d\sigma_L/dt$ in the kinematic regime under investigation. This is because the contributions from \tilde{H} and \tilde{E} , the GPDs which are responsible for the leading-twist structure function σ_L , are very small compared with the contributions from \bar{E}_T and H_T , which contribute to $d\sigma_T/dt$ and $d\sigma_{TT}/dt$. In addition, the transverse cross sections are strongly enhanced by the chiral condensate through the parameter $\mu_\pi = m_\pi^2/(m_u + m_d)$, where m_u and m_d are current quark masses [12].

With the inclusion of the quark-helicity non-conserving chiral-odd GPDs, which contribute primarily to $d\sigma_T/dt$ and $d\sigma_{TT}/dt$ and, to a lesser extent, to $d\sigma_{LT}/dt$, the model of Ref. [33] agrees rather well with the data. Deviations in shape become greater at smaller $-t$ for the unseparated cross section $d\sigma_U/dt$. The behavior of the cross section as $|t| \rightarrow |t|_{min}$ is determined by the interplay between H_T and \bar{E}_T . For the GPDs of Ref. [33] the parameterization was guided by the lattice calculation results of Ref. [35], while Ref. [19] used a GPD Reggeized diquark-quark model to obtain the GPDs. The results in Fig. 23 for the model of Ref. [33] (solid curves), in which \bar{E}_T is dominant, agree rather well with the data. In particular, the structure function σ_U begins to decrease as $|t| \rightarrow |t|_{min}$, showing the effect of \bar{E}_T . In the model of Ref. [19] (dashed curves) H_T is dominant, which leads to a large rise in cross section as $-t$ becomes small so that the contribution of \bar{E}_T relative to H_T appears to be underestimated. One can make a similar conclusion from the comparison between data and model predictions for σ_{TT} . This shows the sensitivity of the measured π^0 structure functions for constraining the transversity GPDs. From Eq. 10 for $d\sigma_T/dt$ and Eq. 11 for $d\sigma_{TT}/dt$ one can conclude that $|d\sigma_{TT}/dt| < d\sigma_T/dt < d\sigma_U/dt$. One sees from Fig. 23 that $-d\sigma_{TT}/dt$ is a sizable fraction of the unseparated cross section while $d\sigma_{LT}/dt$ is very small, which implies that contributions from transversity GPDs play a dominant role in the π^0 electroproduction process.

Fig. 24 shows the extracted structure functions vs. t for all kinematic bins, but this time compared to the GPD calculations of Ref. [33]. While σ_{LT} is very small in all kinematic bins, σ_{TT} remains substantial, which is what one would expect for a transverse pho-

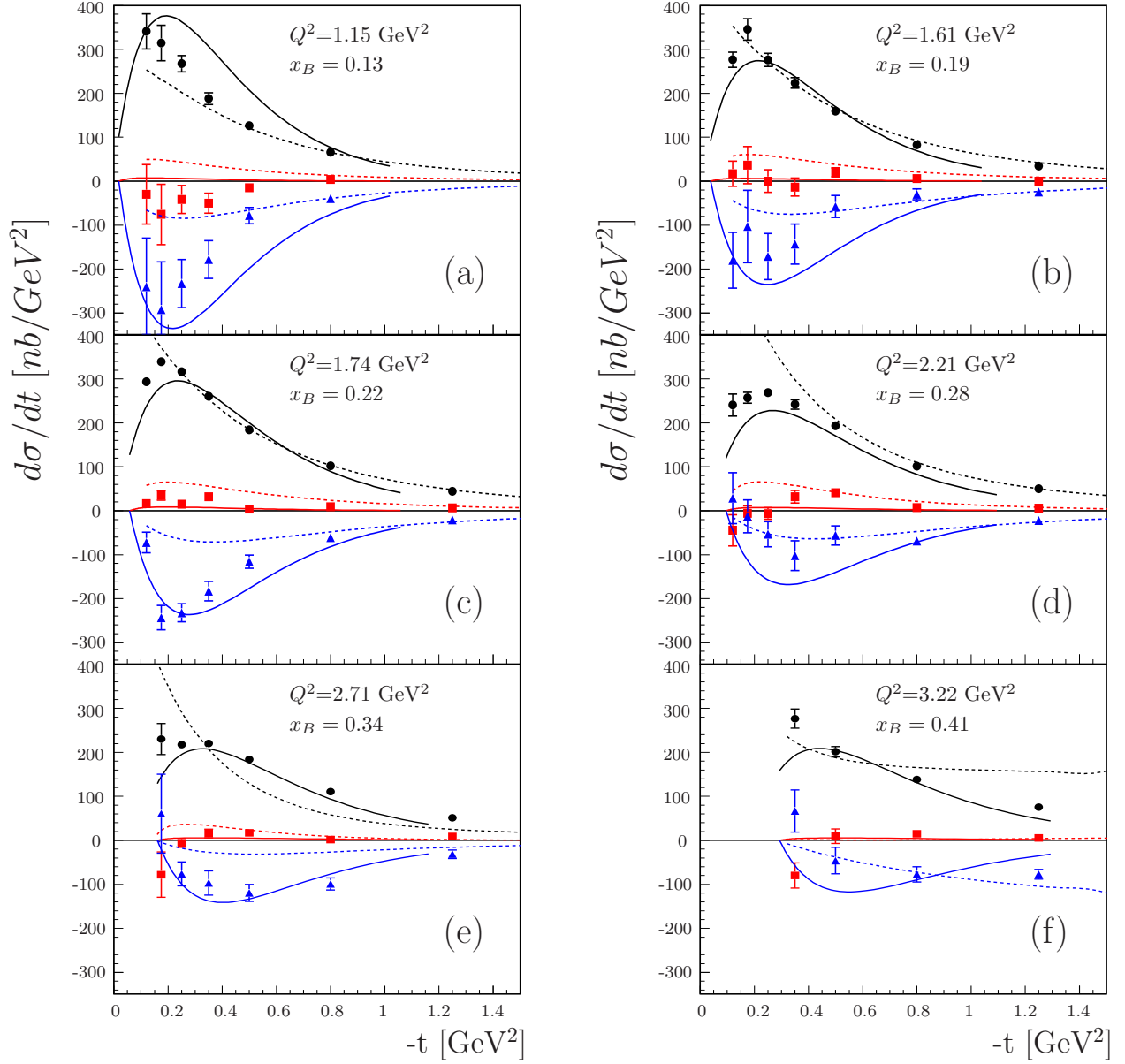


FIG. 23: (Color online) The extracted structure functions vs. t for the bins with the best kinematic coverage and for which there are theoretical calculations. The data and curves are as follows: black (filled circles) - $d\sigma_U/dt = d\sigma_T/dt + \epsilon d\sigma_L/dt$, blue (triangles) - $d\sigma_{TT}/dt$, and red (squares) - $d\sigma_{LT}/dt$. All the structure functions are numerically given in Appendix C. The error bars are statistical only. The point-by-point propagated systematic uncertainties for all the structure functions are given in Appendix C. The curves are theoretical predictions produced with the models of Refs. [33] (solid) and [19] (dashed). In particular: black (positive) - $d\sigma_U/dt (= d\sigma_T/dt + \epsilon d\sigma_L/dt)$, blue (negative) - $d\sigma_{TT}/dt$, and red (small) - $d\sigma_{LT}/dt$

2 **XI. CONCLUSION**

3 Differential cross sections of exclusive neutral-pion
4 electroproduction have been obtained in the few-
5 GeV region at more than 1800 kinematic points in
6 bins of Q^2 , x_B , t and ϕ_π . Virtual photon structure
7 functions $d\sigma_U/dt$, $d\sigma_{TT}/dt$ and $d\sigma_{LT}/dt$ have
8 been obtained. It is found that $d\sigma_U/dt$ and $d\sigma_{TT}/dt$
9 are comparable in magnitude with each other, while
10 $d\sigma_{LT}/dt$ is very much smaller than either. The t -
11 dependent distributions of the structure functions
12 have been compared with calculations based upon
13 the Regge trajectory and handbag approaches. In
14 each case, it is found that the cross sections are dom-
15 inated by transverse photons.

16 In the Regge model [20], in order to account for
17 the magnitude of the cross section, it has been nec-
18 essary to add vector meson rescattering amplitudes
19 (Fig. 22) to the original pole terms and pseudoscalar
20 rescattering amplitudes (Fig. 21).

21 Within the handbag interpretation, there are two
22 independent theoretical calculations [19, 33]. They
23 confirm that the measured unseparated cross sec-
24 tions are much larger than expected from leading-
25 twist handbag calculations which are dominated by
26 longitudinal photons. The same conclusion can be
27 made in an almost model independent way by not-
28 ing that the structure functions $d\sigma_U/dt$ and $d\sigma_{TT}/dt$
29 are comparable to each other while $d\sigma_{LT}$ is quite
30 small in comparison. In the calculation of Ref. [19]
31 the dominant GPD is H_T , which involves a nu-
32 cleon helicity-flip, while that of Ref. [33] has a larger
33 contribution of \bar{E}_T , which involves a nucleon non-
34 helicity-flip. The data at t near t_{min} appear to fa-
35 vor the calculation of Ref. [33]. In Eqs. B21, B22
36 and B23 one can make two observations. First,
37 note that cross section contributions due to \bar{E}_T van-
38 ish as $|t| \rightarrow |t|_{min}$. There is no such constraint on
39 terms involving H_T . The observed $d\sigma_U/dt$ does ap-
40 pear to turn over as $|t| \rightarrow |t|_{min}$, which is expected
41 when the contribution of \bar{E}_T is relatively large, as in
42 Ref. [33]. Second, the structure function $d\sigma_{TT}/dt$,
43 which depends on \bar{E}_T , is relatively large in the data.

44 However, one must be very cautious not to over-
45 interpret the results at this time. Detailed inter-
46 pretations are model dependent and quite dynamic
47 in that they are strongly influenced by new data
48 as they become available. In particular, calcula-
49 tions are in progress to compare the theoretical mod-
50 els with the beam-spin asymmetries obtained earlier
51 with CLAS [16] and longitudinal target spin asym-
52 metries, also obtained with CLAS, which are cur-
53 rently under analysis [36].

54 Extracting $d\sigma_L/dt$ and $d\sigma_T/dt$ and performing
55 new measurements with transversely and longitu-
56 dinally polarized targets would also be very use-
57 ful, and are planned for the future Jefferson Lab at

58 12 GeV. In addition to non-polarized cross sections,
59 which are the subject of the present article, the mea-
60 surement of beam and target spin asymmetries can
61 provide further constraints on the theoretical hand-
62 bag models considered here. Beam-spin asymmetry
63 data at similar kinematic coverage were published
64 by Ref. [16] and in a smaller kinematic range in
65 Ref. [14]. Extensive new CLAS measurements of
66 beam spin, target spin and double-spin asymmetries
67 are currently under analysis. Comparison of these
68 results with the predictions of the handbag models
69 are currently being studied.

70 **Acknowledgments**

We thank the staff of the Accelerator and Physics
Divisions at Jefferson Lab for making the exper-
iment possible. We also thank G. Goldstein, S.
Goloskokov, P. Kroll, J. M. Laget and S. Liuti for
many informative discussions and clarifications of
their work, and making available the results of their
calculations. This work was supported in part by
the U.S. Department of Energy and National Sci-
ence Foundation, the French Centre National de la
Recherche Scientifique and Commissariat à l’Energie
Atomique, the French-American Cultural Exchange
(FACE), the Italian Istituto Nazionale di Fisica Nu-
cleare, the Chilean Comisión Nacional de Investi-
gación Científica y Tecnológica (CONICYT), the
National Research Foundation of Korea, and the UK
Science and Technology Facilities Council (STFC).
The Jefferson Science Associates (JSA) operates the
Thomas Jefferson National Accelerator Facility for
the United States Department of Energy under con-
tract DE-AC05-06OR23177.

71 **Appendix A: Kinematics**

The kinematic variables of the process

$$e(k) + p(p) \rightarrow e'(k') + p'(p') + \pi^0(v)$$

are defined as follows. The four-momenta of the in-
cident and outgoing electrons are denoted by k and
 k' and the four-momentum of the virtual photon q is
defined as $q = k - k'$. In the laboratory system θ is
the scattering angle between the incident and outgo-
ing electrons, with energies E and E' , respectively.
The photon virtuality, given by

$$Q^2 = -q^2 = -(k - k')^2 \approx 4 E E' \sin^2 \frac{\theta}{2} \quad (\text{A1})$$

is positive. The four-momenta of the incident and
outgoing protons are denoted by p and p' . The en-
ergy of the virtual photon is

$$\nu = \frac{p \cdot q}{m_p} = E - E', \quad (\text{A2})$$

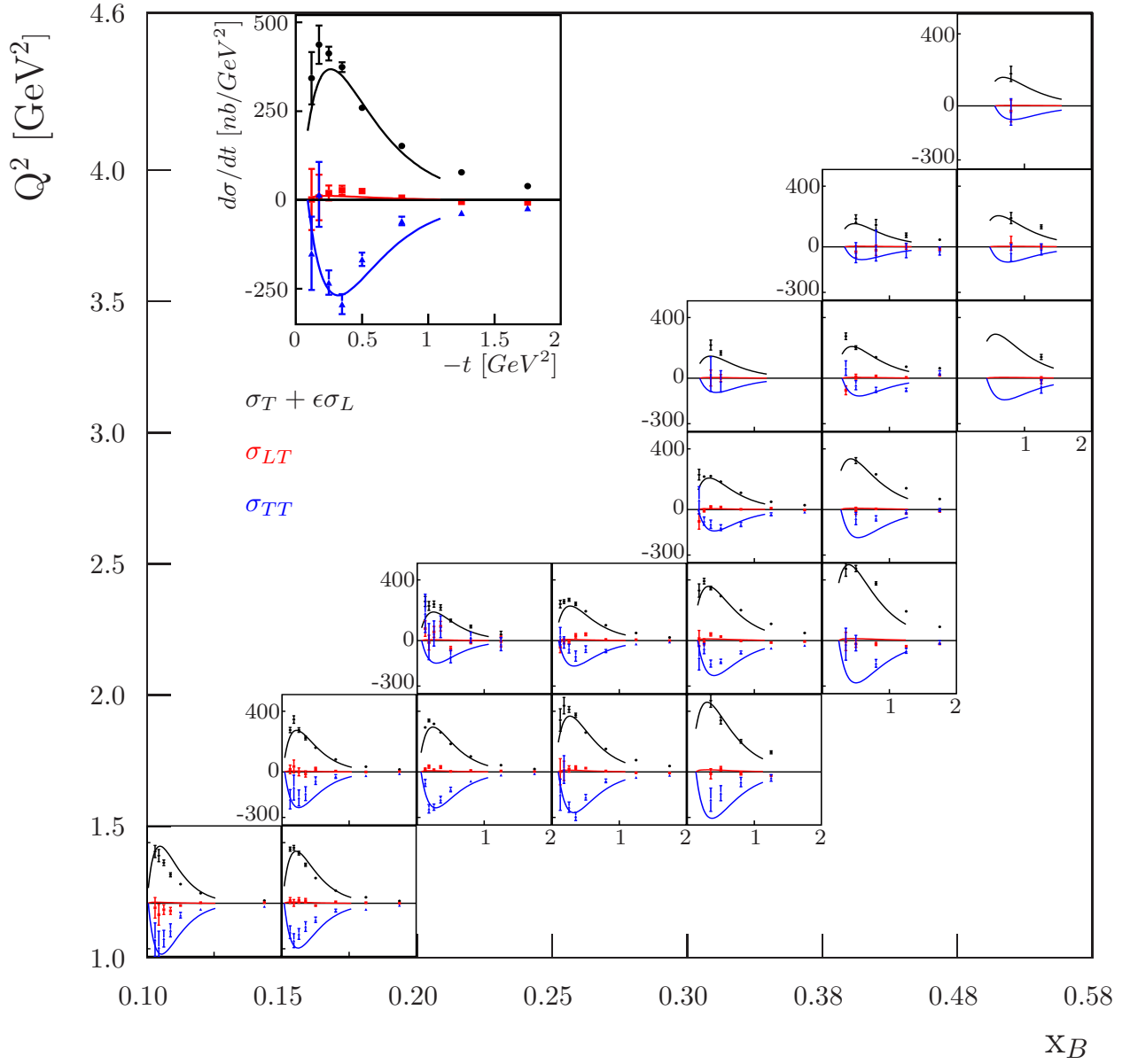


FIG. 24: (Color online) The extracted structure functions vs. t as in Fig. 20 for all kinematic bins. The data and curves are as follows: black (positive)- $d\sigma_U/dt = d\sigma_T/dt + \epsilon d\sigma_L/dt$, blue (negative)- $d\sigma_{TT}/dt$, and red (small)- $d\sigma_{LT}/dt$. All the structure functions are numerically given in Appendix C. The error bars are statistical only. The point-by-point propagated systematic uncertainties are given in the table in Appendix C. The curves are theoretical predictions for these structure functions obtained in the framework of the handbag model by Ref. [33]. As before, black (positive)- $d\sigma_U/dt = d\sigma_T/dt + \epsilon d\sigma_L/dt$, blue (negative)- $d\sigma_{TT}/dt$, and red (small)- $d\sigma_{LT}/dt$.

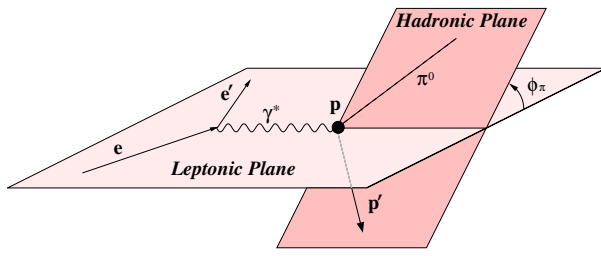


FIG. 25: (Color online) The kinematics of π^0 electroproduction. ϕ_π is the angle between the lepton and hadron planes. The lepton plane is defined by the incident and the scattered electron. The hadron plane is defined by the π^0 and the scattered proton.

where m_p is the proton mass. The Bjorken scaling variable x_B is defined as

$$x_B = \frac{Q^2}{2p \cdot q} = \frac{Q^2}{2m_p \nu}. \quad (\text{A3})$$

The squared invariant mass of the photon-proton system is given by

$$W^2 = (p + q)^2 = m_p^2 + 2m_p \nu - Q^2. \quad (\text{A4})$$

The momentum transfer t to the proton is defined by the relation

$$t = (p - p')^2 = (q - p_\pi)^2, \quad (\text{A5})$$

- 1 where p_π is the four-momentum of the π^0 meson.
- 2 The minimum momentum transfer for a given Q^2
- 3 and W (or x_B) is denoted by t_{min} .

The angle ϕ_π between the leptonic and hadronic planes is defined according to the Trento convention [37] (see Fig. 25).

Appendix B: Helicity amplitudes and Generalized Parton Distributions

Under the assumption of single-photon exchange, the differential cross section of the reaction $ep \rightarrow e'p'\pi^0$ for an unpolarized electron beam and proton target can be written as [12]

$$\frac{d^4\sigma}{dQ^2 dx_B dt d\phi_\pi} = \Gamma(Q^2, x_B, E) \frac{1}{2\pi} \left[\left(\frac{d\sigma_T}{dt} + \epsilon \frac{d\sigma_L}{dt} \right) + \epsilon \cos 2\phi_\pi \frac{d\sigma_{TT}}{dt} + \sqrt{2\epsilon(1+\epsilon)} \cos \phi_\pi \frac{d\sigma_{LT}}{dt} \right], \quad (\text{B1})$$

where $\Gamma(Q^2, x_B, E)$ is the flux of transverse virtual photons and σ_T , σ_L , σ_{TT} and σ_{LT} are the structure functions. They depend in general on the variables Q^2 , x_B and t . The Hand convention [27] was adopted for the definition of the virtual photon flux factor $\Gamma(Q^2, x_B, E)$:

$$\Gamma(Q^2, x_B, E) = \frac{\alpha}{8\pi} \frac{Q^2}{m_p^2 E^2} \frac{1 - x_B}{x_B^3} \frac{1}{1 - \epsilon}, \quad (\text{B2})$$

and α is the standard electromagnetic coupling constant. The variable ϵ represents the ratio of fluxes

of longitudinally and transversely polarized virtual photons and is given by

$$\epsilon = \frac{1 - y - \frac{Q^2}{4E^2}}{1 - y + \frac{y^2}{2} + \frac{Q^2}{4E^2}}, \quad (\text{B3})$$

with $y = p \cdot q / q \cdot k = \nu / E$.

The reduced cross section is defined as

$$\frac{d^2\sigma}{dt d\phi_\pi} = \frac{1}{2\pi} \left[\left(\frac{d\sigma_T}{dt} + \epsilon \frac{d\sigma_L}{dt} \right) + \epsilon \cos 2\phi_\pi \frac{d\sigma_{TT}}{dt} + \sqrt{2\epsilon(1+\epsilon)} \cos \phi_\pi \frac{d\sigma_{LT}}{dt} \right]. \quad (\text{B4})$$

Six independent helicity amplitudes $M_{\mu'\nu'\mu\nu}$ describe the π^0 electroproduction process $\gamma^* p \rightarrow \pi^0 p'$. With reference to Fig. 2, μ and μ' label the helicities

of the virtual photon ($\mu=0,+1,-1$) and π^0 ($\mu' = 0$). The helicities of protons before and after the interaction are labeled ν and ν' , respectively. We will

1 denote “+” for the $\nu = 1/2$ and “-” for $\nu = -1/2$.
 2 The unmeasured helicities of the emitted and absor-
 3 bed quarks are denoted λ and λ' as in Fig. 2.
 4 Four of these amplitudes describe the reaction ini-
 5 tiated by transversely polarized photons: M_{0-++} ,
 6 M_{0--+} , M_{0+++} , M_{0+-+} . The first two correspond
 7 to nucleon helicity flip and the latter two to nucleon
 8 helicity non-flip. There are two amplitudes which
 9 describe the reaction due to longitudinally polar-
 10 ized photons (M_{0+0+} , M_{0-0+}), with nucleon helicity
 11 non-flip and helicity flip, respectively. It is conve-
 12 nient to introduce two new amplitudes with so-called
 13 natural $M_{0\nu'\mu\nu}^N$ and unnatural $M_{0\nu'\mu\nu}^U$ exchanges

$$M_{0\nu'\mu\nu}^N = \frac{1}{2}[M_{0\nu'\mu\nu} + M_{0\nu'-\mu\nu}], \quad (\text{B5})$$

$$M_{0\nu'\mu\nu}^U = \frac{1}{2}[M_{0\nu'\mu\nu} - M_{0\nu'-\mu\nu}]. \quad (\text{B6})$$

14 The former does not change sign upon photon helic-
 15 ity reversal, and the latter changes sign upon photon
 16 helicity reversal.

17 The inverse equations are

$$M_{0\nu'\mu\nu} = M_{0\nu'\mu\nu}^N + M_{0\nu'\mu\nu}^U, \quad (\text{B7})$$

$$M_{0\nu'-\mu\nu} = M_{0\nu'\mu\nu}^N - M_{0\nu'\mu\nu}^U. \quad (\text{B8})$$

For $t' \rightarrow 0$ a helicity amplitude vanishes (at
 least) as $M_{\mu'\nu'\mu\nu} \propto \sqrt{-t'}^{|\mu-\nu-\mu'+\nu'|}$ as a conse-
 quence of angular momentum conservation, where
 $t' = t - t_{min}$. Thus, for transverse photons, for
 nucleon helicity flip ($\nu' = -\nu$) the cross sections
 may remain finite at $t' \rightarrow 0$, while for nucleon he-
 licity non-flip ($\nu' = \nu$), the cross section should
 approach 0 as $t' \rightarrow 0$. According to the findings
 in Refs. [12],[18] and the HERMES measurement of
 the transverse-spin asymmetry A_{UT} , as well as the
 CLAS measurement of the π^0 cross section [13], it
 seems that the following hierarchy of the amplitudes
 for transversely polarized photons holds

$$|M_{0--+}|, |M_{0+++}^U| \ll |M_{0-++}|, |M_{0+++}^N|. \quad (\text{B9})$$

18 The structure functions can be written in terms of
 19 the helicity amplitudes, neglecting the smallest am-
 20 plitudes: in Eq. B9 above.

21 The longitudinal structure function σ_L is con-
 22 nected to longitudinally polarized photons:

$$\frac{d\sigma_L}{dt} = \frac{1}{k} [|M_{0+0+}|^2 + |M_{0-0+}|^2]. \quad (\text{B10})$$

23 The structure function σ_T involves transversely
 24 polarized photons:

$$\begin{aligned} \frac{d\sigma_T}{dt} &= \frac{1}{2k} [|M_{0-++}|^2 + |M_{0--+}|^2 + |M_{0+++}|^2 + |M_{0+-+}|^2] \\ &\simeq \frac{1}{2k} [|M_{0-++}|^2 + 2 |M_{0+++}^N|^2]. \end{aligned} \quad (\text{B11})$$

The structure function σ_{LT} involves the interference between the longitudinal and transverse amplitudes

$$\begin{aligned} \frac{d\sigma_{LT}}{dt} &= -\frac{1}{\sqrt{2}k} \text{Re} [M_{0-0+}^* (M_{0-++} - M_{0--+}) + 2M_{0+0+}^* M_{0+-+}] \\ &\simeq -\frac{1}{\sqrt{2}k} \text{Re} (M_{0-++}^* M_{0-0+}). \end{aligned} \quad (\text{B12})$$

Likewise, the transverse-transverse interference
 cross section σ_{TT} is

$$\begin{aligned} \frac{d\sigma_{TT}}{dt} &= -\frac{1}{k} \text{Re} [M_{0-++}^* M_{0--+} + M_{0+++}^* M_{0+-+}] \\ &\simeq -\frac{1}{k} |M_{0+++}^N|^2. \end{aligned} \quad (\text{B13})$$

The quantity k is the phase space factor, which
 depends on W^2, Q^2, m_p^2 and x_B , and varies approx-
 imately as Q^4 .

$$\begin{aligned}
k &= 16\pi (W^2 - m^2) \sqrt{\Lambda(W^2, -Q^2, m^2)} \\
&= 16\pi Q^2 \left(\frac{1}{x_B} - 1 \right) \sqrt{(W^2 - m^2)^2 + Q^4 + 2W^2 Q^2 + 2Q^2 m^2} \\
&= Q^4 k'
\end{aligned} \tag{B14}$$

1 In the GPD-handbag approximation, exclusive π^0 11
2 electroproduction can be decomposed into a hard 12
3 part, describing the partonic subprocess and a soft 13
4 part that contains the GPDs. This factorization oc- 14
5 curs at large photon virtualities Q^2 and small mo- 15
6 mentum transfer to the nucleon, $-t$. Following the 16
7 notation of Ref. [18], the connection between the he-
8 licity amplitudes and GPDs is

$$M_{0+0+} = \sqrt{1 - \xi^2} \frac{e_0}{Q} \left[\langle \tilde{H} \rangle - \frac{\xi^2}{1 - \xi^2} \langle \tilde{E} \rangle \right] \tag{B15}$$

$$M_{0-0+} = -\frac{e_0}{Q} \frac{\sqrt{-t'}}{2m} \xi \langle \tilde{E} \rangle \tag{B16}$$

$$M_{0-++} = e_0 \frac{\mu_\pi}{Q^2} \sqrt{1 - \xi^2} \langle H_T \rangle \tag{B17}$$

$$M_{0++++}^N = -e_0 \frac{\mu_\pi}{Q^2} \frac{\sqrt{-t'}}{4m} \langle \bar{E}_T \rangle. \tag{B18}$$

9 The variable $\xi \simeq x_B/(2 - x_B)$, $\mu_\pi = m_\pi^2/(m_u + 28$
10 $m_d)$, where m_u and m_d are current quark masses 29

[12] and $\bar{E}_T \equiv 2\tilde{H}_T + E_T$. $\langle F \rangle$ denotes a convolution of GPD F with the hard-scattering kernel, $\mathcal{H}_{\mu'\lambda'\mu\lambda}$, where λ and λ' are the (unmeasured) helicities of the incoming and outgoing quarks, μ is the virtual-photon helicity and $\mu = 0$ is the neutral-pion helicity, and is given by

$$\langle F \rangle \equiv \sum_\lambda \int_{-1}^1 dx \mathcal{H}_{\mu'\lambda'\mu\lambda} F. \tag{B19}$$

17 $\langle H_T \rangle$ arises primarily from nucleon helicity flip pro-
18 cesses, while $\langle \bar{E}_T \rangle$ describes nucleon helicity non-flip
19 processes.

20 Note that a factor $1/Q$ in the longitudinal ampli-
21 tudes and a factor μ_π/Q^2 in the transverse ampli-
22 tudes has been factored in order to explicitly show
23 the leading Q^2 dependence. The convolutions $\langle F \rangle$
24 are still Q^2 dependent due to evolution, the running
25 of α_s and other effects. In the transverse convo-
26 lutions there is also a summation over the parton
27 helicities.

Combining the above finally yields the GPD de-
pendence of the structure functions:

$$\frac{d\sigma_L}{dt} = \frac{4\pi\alpha}{k'} \frac{1}{Q^6} \left\{ (1 - \xi^2) \left| \langle \tilde{H} \rangle \right|^2 - 2\xi^2 \text{Re} \left[\langle \tilde{H} \rangle^* \langle \tilde{E} \rangle \right] - \frac{t'}{4m^2} \xi^2 \left| \langle \tilde{E} \rangle \right|^2 \right\}, \tag{B20}$$

$$\frac{d\sigma_T}{dt} = \frac{4\pi\alpha}{2k'} \frac{\mu_\pi^2}{Q^8} \left[(1 - \xi^2) \left| \langle H_T \rangle \right|^2 - \frac{t'}{8m^2} \left| \langle \bar{E}_T \rangle \right|^2 \right], \tag{B21}$$

$$\frac{\sigma_{LT}}{dt} = \frac{4\pi\alpha}{\sqrt{2}k'} \frac{\mu_\pi}{Q^7} \xi \sqrt{1 - \xi^2} \frac{\sqrt{-t'}}{2m} \text{Re} \left[\langle H_T \rangle^* \langle \tilde{E} \rangle \right], \tag{B22}$$

$$\frac{\sigma_{TT}}{dt} = \frac{4\pi\alpha}{k'} \frac{\mu_\pi^2}{Q^8} \frac{t'}{16m^2} \left| \langle \bar{E}_T \rangle \right|^2. \tag{B23}$$

30

Appendix C: Structure functions

31 The structure functions are presented in this table. The first error is statistical and the second is the
32 systematic uncertainty.

$Q^2,$ GeV^2	x_B	$-t,$ GeV^2	$\frac{d\sigma_T}{dt} + \epsilon \frac{d\sigma_L}{dt},$ nb/GeV^2			$\frac{d\sigma_{LT}}{dt},$ nb/GeV^2			$\frac{d\sigma_{TT}}{dt},$ nb/GeV^2		
1.14	0.131	0.12	341	± 40	± 59	-30	± 68	± 114	-240	± 111	± 156
1.15	0.132	0.17	314	± 40	± 75	-76	± 69	± 126	-292	± 108	± 215
1.15	0.132	0.25	267	± 19	± 15	-42	± 32	± 37	-233	± 55	± 21
1.15	0.132	0.35	188	± 13	± 33	-50	± 23	± 43	-179	± 43	± 66
1.15	0.132	0.49	126.3	± 4.7	± 10	-15.0	± 8.0	± 5.5	-78	± 19	± 8.1
1.15	0.132	0.77	66.0	± 2.0	± 7.9	3.8	± 3.1	± 6.4	-39.8	± 7.8	± 16
1.16	0.133	1.71	17.8	± 2.0	± 1.6	4.3	± 1.2	± 2.0	-21.2	± 6.6	± 7.7
1.38	0.169	0.12	357	± 13	± 35	19	± 19	± 30	-191	± 42	± 47
1.38	0.169	0.17	366	± 15	± 24	2	± 22	± 21	-247	± 46	± 53
1.38	0.169	0.25	331	± 12	± 16	19	± 18	± 17	-202	± 36	± 49
1.38	0.169	0.35	254	± 10	± 13	17	± 15	± 24	-153	± 32	± 25
1.38	0.169	0.49	166.2	± 5.1	± 12	-15.4	± 7.1	± 12	-109	± 18	± 18
1.38	0.169	0.77	83.4	± 3.3	± 4.1	9.7	± 4.4	± 10	-48.5	± 9.6	± 5.4
1.38	0.169	1.21	39.6	± 1.7	± 3.8	4.0	± 1.7	± 1.9	-40.8	± 4.5	± 3.0
1.38	0.170	1.71	15.3	± 1.4	± 1.5	0.81	± 0.80	± 1.6	-13.6	± 4.0	± 5.1
1.61	0.186	0.12	276	± 17	± 46	17	± 29	± 58	-180	± 64	± 71
1.61	0.186	0.18	345	± 25	± 57	36	± 42	± 102	-103	± 82	± 87
1.61	0.187	0.25	276	± 15	± 7.0	0	± 26	± 21	-171	± 52	± 41
1.61	0.187	0.35	223	± 12	± 11	-14	± 20	± 11	-143	± 46	± 46
1.61	0.187	0.49	159.8	± 6.3	± 11	20	± 10	± 11	-58	± 25	± 19
1.61	0.187	0.78	82.4	± 3.2	± 7.1	5.6	± 4.8	± 19	-30	± 12	± 27
1.61	0.187	1.21	34.5	± 2.3	± 3.0	0.1	± 3.3	± 1.7	-24.9	± 6.4	± 6.6
1.61	0.187	1.71	16.0	± 1.9	± 1.6	2.3	± 1.8	± 2.2	-12.2	± 6.2	± 4.6
1.74	0.223	0.25	316.7	± 6.7	± 9.2	14.9	± 8.5	± 19	-232	± 20	± 44
1.75	0.223	0.12	293.3	± 7.8	± 24	16.2	± 9.8	± 12	-72	± 23	± 13
1.75	0.223	0.17	339.3	± 8.9	± 26	35	± 11	± 8.3	-243	± 28	± 26
1.75	0.224	0.35	260.5	± 7.0	± 13	32.1	± 9.2	± 5.0	-183	± 22	± 20
1.75	0.224	0.49	184.4	± 5.0	± 8.6	3.6	± 6.3	± 3.7	-116	± 15	± 20
1.75	0.224	0.78	102.2	± 2.4	± 5.4	9.2	± 3.1	± 5.0	-61.0	± 7.3	± 12
1.75	0.224	1.22	44.5	± 1.4	± 3.0	6.3	± 1.3	± 2.2	-21.2	± 4.1	± 6.0
1.75	0.224	1.72	19.00	± 1.00	± 4.4	2.24	± 0.85	± 3.2	-12.3	± 3.0	± 5.4
1.87	0.270	0.12	342	± 74	± 108	1	± 86	± 72	-150	± 103	± 101
1.87	0.271	0.18	437	± 54	± 90	7	± 64	± 74	16	± 91	± 167
1.87	0.271	0.25	412	± 19	± 32	20	± 21	± 20	-233	± 34	± 39
1.87	0.271	0.35	374	± 14	± 26	27	± 13	± 20	-293	± 28	± 41
1.87	0.271	0.49	259.5	± 7.3	± 13	25.1	± 7.2	± 6.1	-167	± 19	± 14
1.87	0.271	0.78	151.8	± 4.1	± 7.8	6.4	± 4.2	± 5.7	-59	± 12	± 4.6
1.87	0.271	1.22	77.7	± 3.0	± 5.5	-5.7	± 2.3	± 2.8	-36.4	± 7.4	± 5.6
1.87	0.272	1.72	39.2	± 2.1	± 3.5	-7.0	± 1.9	± 1.9	-22.9	± 4.6	± 3.8
1.95	0.313	0.35	470	± 44	± 82	-13	± 34	± 18	-183	± 77	± 58
1.95	0.313	0.49	339	± 23	± 21	21	± 15	± 34	-140	± 50	± 43
1.95	0.313	0.78	202	± 12	± 13	-11.1	± 9.4	± 5.8	-67	± 31	± 23
1.96	0.313	1.22	129.4	± 9.6	± 17	-24.8	± 8.3	± 6.7	-39	± 22	± 21
2.10	0.238	0.12	258	± 33	± 81	79	± 51	± 109	179	± 126	± 218
2.10	0.238	0.35	219	± 18	± 8.1	95	± 31	± 10	91	± 72	± 46
2.10	0.238	0.49	132.5	± 8.9	± 13	-53	± 15	± 9.0	-105	± 41	± 28
2.10	0.238	0.78	92.6	± 8.9	± 9.2	-8	± 13	± 12	21	± 35	± 32
2.10	0.238	1.21	40	± 21	± 16	-6	± 35	± 31	-23	± 43	± 27
2.10	0.239	0.17	228	± 29	± 148	-13	± 49	± 265	-7	± 119	± 268
2.10	0.239	0.25	240	± 20	± 24	57	± 36	± 30	47	± 83	± 106
2.21	0.275	0.12	241	± 25	± 11	-44	± 36	± 9.0	29	± 58	± 17
2.21	0.276	0.17	257	± 12	± 18	-6	± 17	± 13	-13	± 38	± 41
2.21	0.276	0.25	268.8	± 9.8	± 19	-6	± 13	± 20	-54	± 29	± 30
2.21	0.276	0.35	242	± 11	± 11	32	± 14	± 12	-102	± 34	± 22
2.21	0.276	0.49	193.5	± 7.1	± 17	41.1	± 9.4	± 20	-56	± 22	± 47
2.21	0.276	0.78	101.4	± 3.0	± 6.6	7.3	± 4.3	± 7.0	-69	± 10	± 10
2.21	0.277	1.22	50.0	± 2.0	± 3.3	5.8	± 2.3	± 3.9	-22.5	± 6.9	± 2.4
2.21	0.277	1.72	20.8	± 1.5	± 3.1	-0.1	± 1.8	± 2.3	-10.1	± 4.8	± 5.3
2.24	0.332	0.18	330	± 44	± 31	14	± 53	± 37	-114	± 80	± 118
2.24	0.337	0.25	392	± 19	± 44	-8	± 20	± 34	-53	± 34	± 27
2.24	0.338	0.49	293.7	± 6.5	± 15	26.4	± 5.5	± 13	-137	± 14	± 12
2.25	0.337	0.35	346	± 12	± 14	40	± 11	± 12	-152	± 24	± 15
2.25	0.338	0.78	200.8	± 3.8	± 13	-2.1	± 3.3	± 5.0	-78.6	± 9.7	± 10
2.25	0.339	1.22	110.2	± 2.6	± 5.4	-13.3	± 2.3	± 4.2	-50.4	± 6.5	± 6.1
2.25	0.339	1.73	49.9	± 1.7	± 4.6	-6.5	± 1.8	± 5.7	-32.3	± 3.7	± 5.8
2.34	0.403	0.35	472	± 48	± 53	-6	± 60	± 79	-24	± 105	± 210
2.34	0.403	0.49	475	± 20	± 39	-22	± 23	± 27	-17	± 51	± 53
2.34	0.404	0.78	377	± 11	± 17	-22	± 10	± 5.8	-150	± 26	± 19
2.34	0.404	1.22	192.8	± 7.4	± 13	-37.3	± 7.9	± 4.4	-67	± 16	± 43
2.35	0.404	1.73	90.5	± 6.6	± 3.1	-22.4	± 7.4	± 5.7	-13	± 12	± 8.4
2.71	0.336	0.18	230	± 35	± 29	-78	± 52	± 84	60	± 90	± 188
2.71	0.343	0.25	217.3	± 8.1	± 10	-6	± 10	± 4.3	-76	± 27	± 22
2.71	0.343	0.35	220.5	± 8.1	± 8.0	15.5	± 9.8	± 7.6	-97	± 27	± 28
2.71	0.343	0.49	183.8	± 6.0	± 9.4	17.0	± 7.4	± 12	-120	± 19	± 31
2.71	0.343	1.22	51.3	± 2.4	± 4.5	9.0	± 2.7	± 5.0	-31.5	± 9.7	± 16
2.72	0.344	0.78	110.4	± 3.6	± 5.8	1.8	± 4.7	± 5.8	-99	± 14	± 20
2.72	0.344	1.73	28.7	± 1.9	± 3.5	-2.9	± 2.2	± 2.0	-17.2	± 5.6	± 9.2
2.75	0.423	0.50	323	± 19	± 21	-8	± 23	± 16	-60	± 40	± 16
2.75	0.423	0.78	232.4	± 6.9	± 17	4.3	± 6.4	± 16	-58	± 17	± 24
2.75	0.424	1.23	140.7	± 4.9	± 9.0	-25.8	± 5.6	± 5.8	-16	± 13	± 12
2.75	0.424	1.73	69.3	± 4.6	± 2.9	-12.8	± 5.3	± 3.7	-2.7	± 9.6	± 12
3.12	0.362	0.35	219	± 33	± 139	1	± 53	± 213	27	± 114	± 398
3.12	0.362	0.50	167	± 14	± 20	1	± 23	± 59	-21	± 71	± 56
3.22	0.431	0.78	138.4	± 6.2	± 6.5	15.0	± 7.9	± 5.5	-77	± 17	± 16

$Q^2,$ GeV^2	x_B	$-t,$ GeV^2	$\frac{d\sigma_T}{dt} + \epsilon \frac{d\sigma_L}{dt},$ nb/GeV^2			$\frac{d\sigma_{LT}}{dt},$ nb/GeV^2			$\frac{d\sigma_{TT}}{dt},$ nb/GeV^2		
3.23	0.428	0.35	277	± 22	± 15	-80	± 29	± 16	67	± 48	± 20
3.23	0.430	0.50	201	± 12	± 17	10	± 16	± 17	-46	± 30	± 31
3.23	0.432	1.23	75.5	± 3.8	± 9.2	5.6	± 4.3	± 12	-77	± 11	± 32
3.23	0.432	1.73	65.4	± 5.0	± 6.7	18.8	± 5.7	± 6.2	35	± 14	± 15
3.29	0.496	1.23	140	± 17	± 18	-12	± 23	± 9.7	-54	± 45	± 12
3.67	0.451	0.78	145	± 36	± 23	-22	± 35	± 28	8	± 101	± 56
3.67	0.451	1.23	77	± 15	± 1.8	2	± 17	± 2.9	-24	± 48	± 8.8
3.68	0.451	0.49	185	± 26	± 18	-32	± 39	± 29	-38	± 66	± 57
3.68	0.451	1.73	47.0	± 6.9	± 3.9	-14.7	± 9.4	± 7.3	-27	± 27	± 7.9
3.76	0.513	0.78	190	± 37	± 40	24	± 46	± 37	-39	± 56	± 41
3.76	0.514	1.23	132	± 13	± 11	1	± 14	± 8.4	-17	± 37	± 40
4.23	0.539	0.78	178	± 42	± 45	-28	± 60	± 57	-34	± 74	± 64

- [1] X. Ji, Phys. Rev. Lett. **78**, 610 (1997); Phys. Rev. D **55**, 7114 (1997).
- [2] A.V. Radyushkin, Phys. Lett. B **380**, 417 (1996); Phys. Rev. D **56**, 5524 (1997).
- [3] J. C. Collins and A. Freund, Phys. Rev. D **59**, 074009 (1999).
- [4] J. C. Collins, L. Frankfurt and M. Strikman, Phys. Rev. D **56**, 2982 (1997).
- [5] D. Mueller, D. Robaschik, B. Geyer, F.M. Dittes and J.D. Horejsi, Fortsch. Phys. **42**, 101 (1994).
- [6] C. M. Camacho *et al.* (HALL-A Collaboration), Phys. Rev. Lett. **97**, 262002 (2006).
- [7] P. Hoodbhoy and X. Ji, Phys. Rev. D **58**, 054006 (1998).
- [8] M. Diehl, Phys. Rep. **388**, 41 (2003) and references within.
- [9] K. Goetze, M. V. Polyakov and M. Vanderhaeghen, Prog. Part. Nucl. Phys. **47**, 401 (2001).
- [10] M. I. Eides, L. L. Frankfurt and M. I. Strikman, Phys. Rev. D **59**, 114025 (1999).
- [11] H. W. Huang and P. Kroll, Eur. Phys. J. C **17**, 423 (2000).
- [12] S. V. Goloskokov and P. Kroll, Eur. Phys. J. C **65**, 137 (2010).
- [13] I. Bedlinskiy *et al.* (CLAS Collaboration), Phys. Rev. Lett. **109**, 112001 (2012).
- [14] E. Fuchey *et al.* (HALL-A Collaboration), Phys. Rev. C **83**, 025201 (2011).
- [15] A. Airapetian *et al.* (HERMES Collaboration), Phys. Lett. B **682**, 345 (2010).
- [16] R. De Masi *et al.* (CLAS Collaboration), Phys. Rev. C **77**, 042201 (2008).
- [17] S. Ahmad, G. R. Goldstein and S. Liuti, Phys. Rev. D **79**, 054014 (2009).
- [18] S. V. Goloskokov and P. Kroll, Eur. Phys. J. A **47**, 112 (2011).
- [19] G. Goldstein, J. O. Gonzalez-Hernandez and S. Liuti, Phys. Rev. D **84**, 034007 (2011); Int. J. Mod. Phys. Conf. Ser. **20**, 222 (2012); J. Phys. G: Nucl. Part. Phys. **39** 115001 (2012).
- [20] J.-M. Laget, Phys. Lett. B **695**, 199 (2011) and references within.
- [21] B. A. Mecking *et al.*, Nucl. Inst. and Meth. A **503**, 513 (2003).
- [22] M. D. Mestayer *et al.*, Nucl. Inst. and Meth. A **449**, 81 (2000).
- [23] G. S. Adams *et al.*, Nucl. Inst. and Meth. A **465**, 414 (2001).
- [24] E. S. Smith *et al.*, Nucl. Inst. and Meth. A **432**, 265 (1999).
- [25] M. Amarian *et al.*, Nucl. Inst. and Meth. A **460**, 239 (2001).
- [26] A. Afanasev, I. Akushevich, V. Burkert and K. Joo, Phys. Rev. D **66**, 074004 (2002).
- [27] L. Hand, Phys. Rev. **129**, 1834 (1963).
- [28] See Supplemental Material at [LINK WILL BE PROVIDED BY PRC] for differential cross sections for exclusive π^0 electroproduction $\frac{d^2\sigma}{dt d\phi_\pi}(\gamma^* p \rightarrow \pi^0 p)$.
- [29] S. A. Morrow *et al.* (CLAS Collaboration), Eur. Phys. J. A **39**, 5 (2009).
- [30] M. Burkardt, e-Print: arXiv:0711.1881.
- [31] J. M. Laget, Phys. Rev. C **73**, 044003 (2006).
- [32] J. M. Laget, Phys. Lett. B **685**, 146 (2010).
- [33] S. V. Goloskokov and P. Kroll, Eur. Phys. J. A **47**, 112 (2011).
- [34] M. Diehl and Ph. Haegler, Eur. Phys. J. C **44**, 87 (2005).
- [35] M. Gockeler *et al.* [QCDSF Collaboration and UKQCD Collaboration], Phys. Rev. Lett. **98**, 222001 (2007).
- [36] A. Kim *et al.* (CLAS Collaboration), in preparation, private communication.
- [37] A. Bacchetta, U. D'Alesio, M. Diehl, C.A. Miller, Phys. Rev. D **70**, 117504 (2004).